

RESEARCH ARTICLE

The histone H4 lysine 20 demethylase DPY-21 regulates the dynamics of condensin DC binding

Laura Breimann^{1,2,3,*}, Ana Karina Morao^{1,*}, Jun Kim¹, David Sebastian Jimenez¹, Nina Maryn¹, Krishna Bikkasani¹, Michael J. Carrozza¹, Sarah E. Albritton¹, Maxwell Kramer¹, Lena Annika Street¹, Kustrim Cerimi², Vic-Fabienne Schumann², Ella Bahry², Stephan Preibisch^{2,4}, Andrew Woehler² and Sevinç Ercan^{1,2,†}

ABSTRACT

Condensin is a multi-subunit structural maintenance of chromosomes (SMC) complex that binds to and compacts chromosomes. Here, we addressed the regulation of condensin binding dynamics using *Caenorhabditis elegans* condensin DC, which represses X chromosomes in hermaphrodites for dosage compensation. We established fluorescence recovery after photobleaching (FRAP) using the SMC4 homolog DPY-27 and showed that a well-characterized ATPase mutation abolishes DPY-27 binding to X chromosomes. Next, we performed FRAP in the background of several chromatin modifier mutants that cause varying degrees of X chromosome derepression. The greatest effect was in a null mutant of the H4K20me2 demethylase DPY-21, where the mobile fraction of condensin DC reduced from ~30% to 10%. In contrast, a catalytic mutant of *dpy-21* did not regulate condensin DC mobility. Hi-C sequencing data from the *dpy-21* null mutant showed little change compared to wild-type data, uncoupling Hi-C-measured long-range DNA contacts from transcriptional repression of the X chromosomes. Taken together, our results indicate that DPY-21 has a non-catalytic role in regulating the dynamics of condensin DC binding, which is important for transcription repression.

KEY WORDS: Condensin, Transcription, Histone modifications, FRAP, Hi-C, *C. elegans*

INTRODUCTION

The evolutionarily conserved structural maintenance of chromosomes (SMC) complexes use the energy from ATP hydrolysis to regulate chromosome structure in various nuclear processes (Hirano, 2016). Condensin is an SMC complex that


regulates DNA compaction for chromosome segregation during cell division and genome organization for transcription regulation during interphase (Paul et al., 2018a). The current model of how condensins compact DNA involves a process called loop extrusion (Cacciatore and Rowland, 2019; Goloborodko et al., 2016). Unlike a related SMC complex called cohesion, the proteins and chromatin factors that regulate the dynamics of condensin binding are less clear (Paul et al., 2018b). Here, we addressed this question using the *Caenorhabditis elegans* dosage compensation system, where X chromosome-specific condensin binding and function is better understood and serves as a model for the metazoan condensins (Albritton and Ercan, 2018).

In *C. elegans*, X chromosome dosage compensation is mediated by a specialized condensin that forms the core of the dosage compensation complex (DCC) (Meyer, 2005). This X chromosome-specific condensin (hereafter referred to as condensin DC) is distinguished from the canonical condensin I by a single SMC-4 variant called DPY-27 (Csankovszki et al., 2009). The current model of condensin DC binding to the X chromosomes posits that SDC-2, along with SDC-3 and DPY-30, initiates X chromosome-specific binding of the complex to a small number of recruitment elements on the X (*rex*) (Albritton et al., 2017; Csankovszki et al., 2004; Jans et al., 2009). Robust binding of condensin DC to the X chromosomes requires multiple *rex* elements (Albritton et al., 2017). The complex binding is enriched at active promoters, enhancers and other accessible sites (Ercan et al., 2009; Street et al., 2019). Similar to other SMC complexes, condensin DC likely translocates along DNA through loop extrusion and mediates long-range DNA contacts enriched on the X chromosomes (Anderson et al., 2019; Crane et al., 2015; Jimenez et al., 2021 preprint). A subset of the strong *rex* sites also serve as blocks to condensin DC movement, insulating DNA contacts and forming loop-anchored topologically associating domains (TADs) (Crane et al., 2015; Jimenez et al., 2021 preprint).

Condensin DC physically interacts with DPY-21 (Yonker and Meyer, 2003), a Jumonji domain-containing histone demethylase that converts dimethylated histone H4 lysine 20 (H4K20me2) to monomethylated histone H4 lysine 20 (H4K20me1) (Brejc et al., 2017), resulting in increased levels of H4K20me1 and reduced levels of di- and tri-methylated histone H4 lysine 20 (H4K20me2/3) on the X chromosome (Vielle et al., 2012; Wells et al., 2012). This leads to deacetylation of histone H4 at lysine 16 mediated by SIR-2.1 (Wells et al., 2012). As a result, the two dosage compensated X chromosomes in hermaphrodites contain higher levels of H4K20me1 and lower levels of histone H4 lysine 16 acetylation (H4K16ac). Furthermore, condensin DC and *dpy-21* are also required for lower levels of histone H3 lysine 27 acetylation (H3K27ac) on the X chromosome (Street et al., 2019). An increase

¹Department of Biology, Center for Genomics and Systems Biology, New York University, New York, NY 10003, USA. ²Berlin Institute for Medical Systems Biology, Max Delbrück Center for Molecular Medicine, 10115 Berlin, Germany. ³Institute for Biology, Humboldt University of Berlin, 10099 Berlin, Germany. ⁴Janelia Research Campus, Howard Hughes Medical Institute, Ashburn, VA 20147, USA. *These authors contributed equally to this work

†Authors for correspondence (se71@nyu.edu; laura.breimann@mdc-berlin.de)

 L.B., 0000-0001-7702-5749; A.K.M., 0000-0003-2194-8071; J.K., 0000-0001-9473-3093; D.S., 0000-0003-0943-9063; N.M., 0000-0002-0975-3354; K.B., 0000-0002-4000-1863; S.E.A., 0000-0001-6093-9560; M.K., 0000-0002-1643-0756; L.A.S., 0000-0002-5473-6713; K.C., 0000-0003-0775-3032; V.F.S., 0000-0003-0227-7428; E.B., 0000-0002-6358-2576; S.P., 0000-0002-0276-494X; A.W., 0000-0001-5157-9313; S.E., 0000-0001-7297-1648

This is an Open Access article distributed under the terms of the Creative Commons Attribution License (<https://creativecommons.org/licenses/by/4.0>), which permits unrestricted use, distribution and reproduction in any medium provided that the original work is properly attributed.

Handling Editor: Caroline Hill

Received 21 April 2021; Accepted 29 November 2021

of H4K20me1 and decreased acetylation mirror the histone modification changes on metazoan mitotic chromatin (Schmitz et al., 2020), providing a link between canonical condensin and condensin DC binding to chromatin.

In this study, we analyzed the effect of several mutants that regulate H4K20 methylation and H4K16 acetylation on the dynamics of condensin DC binding using fluorescence recovery after photobleaching (FRAP). We established FRAP in *C. elegans* intestine cells using a GFP-tagged DPY-27 and validated the system by demonstrating that condensin DC mobility increases upon depletion of its recruiter SDC-2. We found that introducing a well-characterized mutation in the ATPase domain of DPY-27 eliminated its binding to the X chromosomes, as measured by FRAP and ChIP-seq. Mutants that regulate H4K20 methylation and H4K16 deacetylation showed subtle effects on condensin DC binding dynamics as measured by FRAP. The most substantial effect was in the *dpy-21* null mutant, in which the fraction of mobile DPY-27 was reduced from ~30% to ~10%. Unlike the null mutant, the *dpy-21(JmjC)* catalytic mutant did not affect condensin DC mobility, suggesting that the role of DPY-21 in regulating condensin DC binding dynamics is non-catalytic. We performed Hi-C analysis in the *dpy-21* null mutant and *dpy-21(JmjC)* catalytic mutant and observed little change in long-range DNA contacts, including those between the *rex* sites (Brejc et al., 2017). Taken together, our results suggest that DPY-21 has a non-catalytic role in regulating the dynamics of condensin DC binding to the X chromosomes, which is important for its function in transcription repression.

RESULTS

FRAP measurement of condensin DC binding *in vivo*

To analyze condensin DC binding *in vivo*, we used FRAP, which has been used previously to measure functionally relevant dynamics of condensin binding in budding yeast (Thadani et al., 2018) and of condensin I and II complexes in human cells (Gerlich et al., 2006; Walther et al., 2018). We set up the FRAP system using DPY-27, the SMC4 homolog that distinguishes condensin DC from condensin I (Fig. 1A). To fluorescently label DPY-27, we added a Halo tag endogenously at the C terminus using CRISPR/Cas9 genome editing. Unlike *dpy-27* mutants, which have lethal or dumpy phenotypes, the resulting animals were phenotypically wild type, indicating that the tagged protein complements protein function. This was also supported by subnuclear localization of DPY-27::Halo, which is typical of X chromosome-specific localization of the DCC (Fig. 1B) (Csankovszki et al., 2004; Jans et al., 2009). DPY-27::Halo did not photobleach sufficiently in our hands, and endogenous tagging with GFP did not produce a strong signal. Thus, we turned to expressing a GFP-tagged copy of DPY-27 using a heat-inducible promoter to perform FRAP. First, we characterized the expression of the transgene by incubating adults at 35°C for 1 h then moving them to the normal growth temperature of 20°C. After 3 h at 20°C, excess DPY-27::GFP was visible across the nuclei, but after 8 h, localization was constrained to a subnuclear domain, suggesting that the remaining protein bound specifically to the X chromosomes (Fig. 1C).

We validated that DPY-27::GFP forms a complex and binds to DNA as expected in three ways. First, we analyzed the localization of DPY-27::GFP after 8 h of recovery in intestine cells in the presence of the Halo-tagged endogenous protein. DPY-27::GFP colocalized with DPY-27::Halo, indicating proper localization (Fig. 1B; Fig. S1A). Second, DPY-27::GFP was detected in immunoprecipitates of DC subunits, supporting the complex-formation capabilities of DPY-27::GFP (Fig. 1D;

Fig. S1B). Third, DPY-27::GFP was enriched on the X chromosomes, and the ChIP-seq binding pattern followed that of DPY-26, the kleisin subunit of condensin DC (Fig. S1C; Fig. 2C).

We chose intestine cells for performing FRAP because the nuclei of these cells are large due to polyploidy, and subnuclear localization of the complex is easily detected (Fig. 1E). Previous studies have also used these cells to analyze condensin DC binding by immunofluorescence (Brejc et al., 2017; Csankovszki et al., 2004; Wells et al., 2012; Yonker and Meyer, 2003). In addition, controlling DPY-27::GFP expression in intestines was easier than in embryos, where the nuclei were small (Fig. S1D) and there was variability in heat-induced expression of DPY-27::GFP (Fig. S1E).

To further validate the FRAP assay in intestine cells, we compared DPY-27::GFP recovery to that of free GFP with a nuclear localization signal (NLS::GFP) and histone H2B::GFP (Fig. 1E–H). FRAP allows two types of quantitative measurement of protein mobility. First is the proportion of mobile molecules, which is calculated from the percentage of the recovered signal at the bleached area by replacement of bleached molecules. Second is the recovery speed, where diffusion is indicated by a fast recovery, transient binding results in a slower recovery, and stable binding is observed as an increase in the immobile fraction (Mueller et al., 2013). As expected, the mobile fraction of free GFP (Fig. 1G) was much higher than that of histone H2B. H2B::GFP minimally recovered during the experiment time frame and was therefore excluded from the half-life recovery plot (Fig. 1H). This result is in line with FRAP experiments in human cell lines reporting a mobile fraction for most H2B–GFP of 4% with a half time (T-half) of recovery of over 2 h (Kimura and Cook, 2001).

The DPY-27::GFP mobile fraction was ~30%, and the half time of recovery was ~2.6 s. FRAP results from different experimental setups with different imaging settings and analysis strategies can differ significantly (Mazza et al., 2012). However, the time scale for DPY-27::GFP recovery is similar to recovery half times reported in *Saccharomyces cerevisiae* for Smc4, ~2 s and ~6 s in G1 and M phase, respectively (Thadani et al., 2018), and different from residence times reported for human condensin I and II (Gerlich et al., 2006; Walther et al., 2018). During metaphase, human condensin I has a residence time of ~3 min with a mobile fraction of 80% (Gerlich et al., 2006; Walther et al., 2018). Condensin II, which binds to chromatin throughout the cell cycle, has a residence time of more than 5 min with a mobile fraction of 40% (Gerlich et al., 2006; Walther et al., 2018). Our results indicate that DPY-27 has a higher chromosome-bound fraction than human condensin I and II but has comparable recovery half times to those reported in yeast.

A conserved mutation of the DPY-27 ATPase domain eliminates its binding in the presence of the wild-type protein

If FRAP can measure changes in condensin DC binding dynamics, we reasoned that knockdown of the condensin DC recruiter SDC-2, and a well-characterized ATP hydrolysis mutation that is known to eliminate the function of other SMC4 homologs, should observably affect DPY-27 binding dynamics. In condensins, the two heads of SMC2 or SMC4 form the two halves of the ATPase domain; each head interacting with the other in the presence of an ATP molecule, hydrolysis of which dissociates the heads (Hirano, 2016). To test whether the ATP hydrolysis by DPY-27 is necessary for its binding to DNA, we inserted a Walker B mutation (E to Q; Fig. 2A) that nearly eliminates ATP hydrolysis in human (Vian et al., 2018), *Xenopus* (Kinoshita et al., 2015), yeast (Hirano and Hirano, 2004; Thadani et al., 2018) and chicken (Hudson et al., 2008). Unlike wild-type DPY-27::GFP, DPY-27(EQ)::GFP failed to show

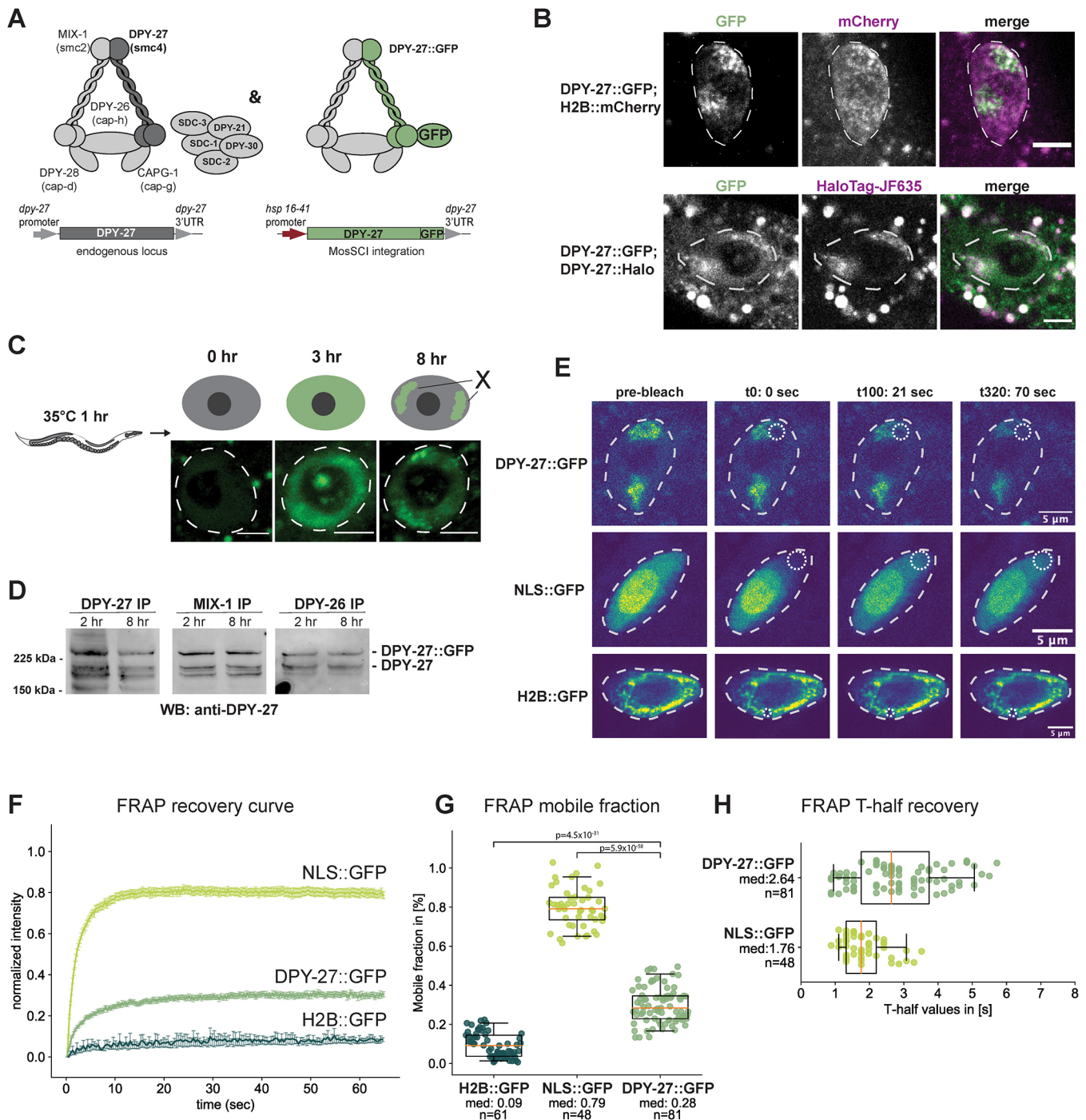


Fig. 1. See next page for legend.

subnuclear enrichment indicative of localization to the X chromosome (Fig. 2B; Fig. S2D,E). The conclusion that ATP hydrolysis by DPY-27 is required for its localization to the X chromosome was further supported by ChIP-seq analysis of DPY-27::GFP and DPY-27(EQ)::GFP in embryos. Thus, unlike wild-type DPY-27::GFP, the ATPase mutant failed to bind to the X chromosomes in the presence of endogenous DPY-27 (Fig. 2C; Fig. S2A).

Next, we asked whether the ATPase mutant improperly interacted with chromatin and showed a dominant-negative effect. The mobility of DPY-27(EQ)::GFP was slightly lower than that of unbound

DPY-27::GFP generated by knockdown of the condensin DC recruiter SDC-2, thus the mutant might incorrectly associate with chromatin (Fig. 2D; Fig. S2B). Supporting a small dominant-negative effect, mRNA-seq analysis of embryos expressing DPY-27(EQ)::GFP showed slightly higher X chromosome upregulation than those expressing DPY-27::GFP (Fig. S2C). X chromosome upregulation upon wild-type DPY-27::GFP expression may be due to dosage imbalance within the complex. Additional X chromosome upregulation in the EQ mutant may be due to a negative effect on DPY-27, as proposed for SMCL-1, an SMC-like protein with an ATPase hydrolysis mutation (Chao et al., 2017).

Fig. 1. FRAP analysis of condensin DC binding. (A) Left panel illustrates condensin DC along with the rest of the DCC subunits. The right panel indicates the expression of GFP-tagged DPY-27 under the control of a heat shock-inducible promoter at the chromosome II MosSCI site. (B) DPY-27::GFP subnuclear localization to the X chromosomes in intestinal cells 8 h after heat-induced expression (top row) was validated by colocalization with the endogenously tagged DPY-27::Halo stained with JF635 HaloTag ligand (bottom row). Nuclei are outlined by white dashed lines. Images are representative of three biological replicates with a minimum of 20 images. Scale bars: 5 μ m. (C) Illustration of the heat-shock protocol (top). Young adult worms were heat shocked for 1 h at 35°C, and fluorescence was followed in the large intestinal cells. DPY-27::GFP subnuclear localization indicative of X chromosome binding is apparent after 8 h of recovery. Representative example images from a total of three biological replicates with a minimum of 30 images are shown for each time point, with the nuclear area marked using a white dashed line. Scale bars: 5 μ m. (D) DPY-27::GFP interaction with condensin DC subunits was validated by co-immunoprecipitation with MIX-1 and DPY-26. Young adult worms were used for immunoprecipitation (IP) either 2 h or 8 h after heat shock at 35°C for 1 h and analyzed by western blotting (WB) using an anti-DPY-27 antibody. The intensity of the GFP-tagged DPY-27 and endogenous protein bands in the DPY-27 IP lane indicates the relative abundance of each protein. The intensity of the GFP-tagged DPY-27 and the endogenous protein bands in the other lanes indicates the relative interaction of endogenous and DPY-27::GFP with the immunoprecipitated subunit. Blots are representative of three experiments. (E) FRAP sequence for intestine nuclei of adult *C. elegans* worms expressing either DPY-27::GFP, NLS::GFP or H2B::GFP. The first column of images depicts the first image of the pre-bleach series (a total of 20 images). The second column shows the first image after the single point bleach, with the bleached area indicated by the dotted circle. The third and fourth columns depict two time points after the bleach point: t100 (21 s) and t320 (70 s), respectively. Nuclei are outlined by white dashed lines. (F) Mean FRAP recovery curves from worms expressing wild-type DPY-27::GFP, H2B::GFP or NLS::GFP. Data are mean \pm s.e.m. Numbers of bleached single intestine nuclei (from at least three biological replicates) for each experiment are $n=81$ for DPY-27::GFP, $n=48$ for NLS::GFP and $n=61$ for H2B::GFP. (G) Mobile fractions for the different GFP-tagged proteins or free GFP. The mobile fraction is the lowest for H2B::GFP and the highest for NLS::GFP. The mobile fraction for DPY-27::GFP is $\sim 28\%$. *P*-values are from an two-tailed independent two-sample *t*-test. (H) FRAP half time recovery (T-half) values for the bleach curves shown in Fig. 1F. The half time recovery for NLS::GFP shows a shorter diffusion time than DPY-27::GFP. H2B::GFP is not shown due to the very low recovery of the fluorescence signal during the experimental time frame. Boxplots in G and H show the median (line), interquartile range (box) and whiskers at the 5th and 95th percentile of the dataset. The median values (med) and number of nuclei analyzed are shown for each group.

To test whether the failure of DPY-27(EQ)::GFP to bind is due to its inability to form a complex, we performed co-immunoprecipitation experiments in embryos and young adults (Fig. 2E; Fig. S2F). We noticed that both wild-type and EQ-mutant DPY-27::GFP interacted well with MIX-1 (an SMC2 homolog). However, DPY-27::GFP coimmunoprecipitated better with DPY-26 (kleisin subunit of condensin I and condensin DC) compared to DPY-27(EQ)::GFP, suggesting that the ATPase mutation affects SMC–kleisin interaction. Lack of X chromosome-specific localization measured by both imaging (Fig. 2B) and ChIP-seq (Fig. 2C) suggests that a combination of inability to form a complex and reduced ATP hydrolysis eliminates binding of DPY-27(EQ)::GFP.

Recombinant DPY-28 HEAT-repeat domain binds to histone H3 and H4 peptides *in vitro*

We wondered whether histone modifications on chromatin regulate dynamics of condensin binding and took a candidate approach, considering histone modifiers that have been shown to have a role in *C. elegans* dosage compensation: SET-1 H4K20me1 and SET-4

H4K20me2 methyltransferases, DPY-21 H4K20me2 demethylase and SIR-2.1 H4K16 deacetylase (Kramer et al., 2015; Wells et al., 2012) (Fig. 3A). A catalytic mutant of DPY-21, *dpy-21(JmjC)*, which has near elimination of DPY-21 demethylase activity, also shows dosage compensation defects, albeit at a lower level than the null mutant (Brejc et al., 2017). Similarly, we found that the *sir-2.1* null mutant also displays slight X derepression (Fig. S3A) and dumpiness, a phenotype indicating dosage compensation problems (Fig. S3B).

We first considered how condensin DC might interact with histones (Fig. 3B). HEAT repeats, a helical protein structural motif that mediates protein and DNA interactions, are present in the CAPD and CAPG subunits of condensins (Yoshimura and Hirano, 2016). Recombinant HEAT-repeat domains from condensin II interact with histone H4 peptides monomethylated at lysine 20 (Liu et al., 2010). We asked whether the HEAT repeats in condensin I and condensin DC also interact with histone tails. The HEAT repeats in CAPG-1 are predicted to bind DNA (Kschonsak et al., 2017). Thus, we focused on DPY-28 (a CAP-D2 homolog) and identified its HEAT repeat domain using homology to human CAP-D2 (also known as NCAPD2) and Pfam HEAT repeat (PF02985) predictions (Fig. 3C).

We performed an *in vitro* in-solution peptide binding assay using the recombinant DPY-28 HEAT-repeat domain (Fig. S3C) and 23-amino-acid N-terminal histone H4 peptides that were either unmodified or mono-, di- or tri-methylated at lysine 20, as well as unmodified and tetra-acetylated histone H3 (K4, K9, K14 and K18) and H4 (K5, K8, K12 and K16) peptides (Fig. S3D). Recombinant DPY-28 HEAT-repeat domain interacted with unmodified 23-amino-acid H4 and 20-amino-acid H3 N-terminal peptides (Fig. 3D). Tetra-acetylation of H3 and H4 peptides, and trimethylation of histone H4 peptides at lysine 20 reduced the interaction (Fig. 3D). Thus, histone modifications have the potential to regulate condensin DC interaction with chromatin.

SET-4, SIR-2.1 and catalytic activity of DPY-21 do not regulate condensin DC binding

While there is a potential for condensin DC interaction with histones, previous studies have shown little effect of chromatin modifier mutations on condensin DC localization, except a slight reduction of DPY-27 ChIP-seq signal across promoters in the *dpy-21* null mutant (Brejc et al., 2017; Kramer et al., 2015; Vielle et al., 2012; Wells et al., 2012). We performed DPY-27 ChIP-seq in *sir-2.1* null embryos and, again, did not see a significant difference in condensin DC binding to the X chromosomes compared to that in wild-type embryos (Fig. 3E; Fig. S3E). To further rule out the effect of chromatin modifiers, we used X;V fusion chromosomes, where the gradual spreading of condensin DC into the autosomal region may be more sensitive for detecting binding changes (Ercan et al., 2009; Street et al., 2019). We were unable to obtain a homozygous X;V fusion in the *dpy-21* null background, thus we analyzed *dpy-21(JmjC)* and *set-4* null mutants (Fig. 3F; Fig. S3F). In wild-type, *dpy-21(JmjC)* and *set-4* null backgrounds, ChIP-seq replicates showed variable changes in condensin DC spreading into the autosomal region (Fig. 3G). Thus, *set-4*, *sir-2.1* and the catalytic activity of DPY-21 do not regulate condensin DC binding as measured by ChIP-seq.

DPY-21 has a non-catalytic activity that increases the mobile fraction of condensin DC

Since the histone modifiers showed little effect on condensin DC binding as measured by ChIP-seq, we used our established FRAP

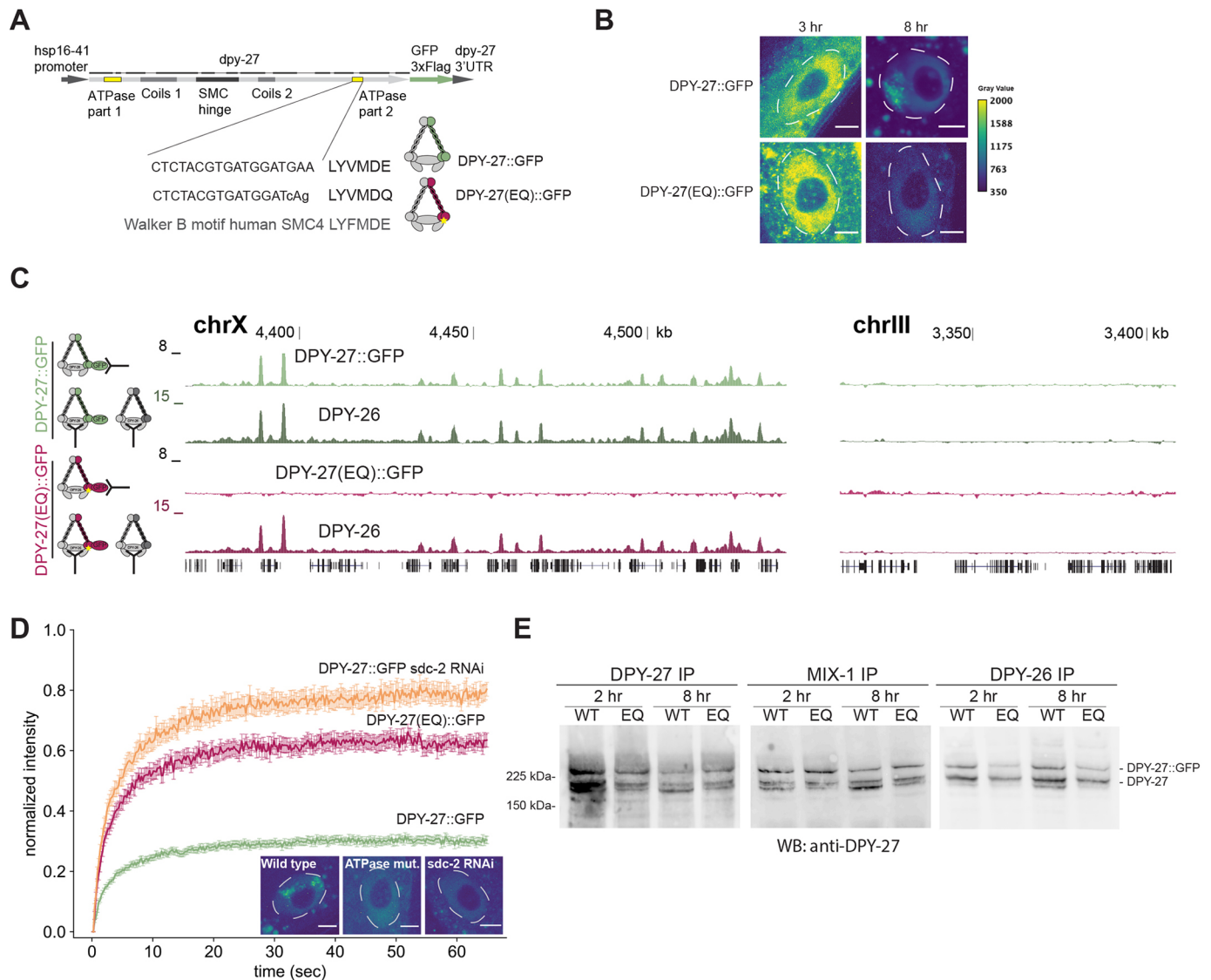


Fig. 2. The effect of a conserved SMC ATPase mutation on DPY-27 binding, function, protein stability and complex formation. (A) Sequence encoding heat shock-inducible GFP-tagged DPY-27(EQ). The DNA sequence coding for the conserved Walker B motif and the E-to-Q mutation are shown below. (B) Localization of the wild-type and EQ ATPase mutant DPY-27::GFP proteins in intestine cells. Adults were heat shocked at 35°C for 1 h and recovered for either 3 h or 8 h. Unlike DPY-27::GFP, the ATPase EQ mutant did not show subnuclear localization. Nuclei are outlined by white dashed lines. Images are representative of three replicates (quantified in Fig. S3E). Scale bars: 5 μ m. (C) ChIP-seq analysis of wild-type and ATPase mutant DPY-27::GFP using an anti-GFP antibody in embryos. ChIP against DPY-26 was used as a positive control in the same extracts. Unlike the wild-type protein, the ATPase mutant failed to bind to the X chromosome (chrX), and both did not localize to the autosomes. A representative region from chromosome III is shown in the right panel. ChIP profiles show normalized read coverage (y-axis) for representative regions on chromosome X and III in a UCSC genome browser snapshot. Data are representative of three replicate experiments. (D) Mean FRAP recovery curves from DPY-27::GFP, DPY-27(EQ)::GFP and DPY-27::GFP upon SDC-2 RNAi. FRAP was performed ~8 h after the heat shock. Data are mean \pm s.e.m. Numbers of bleached single intestine nuclei (from at least three biological replicates) for each experiment are $n=81$ for DPY-27::GFP, $n=37$ for DPY-27(EQ)::GFP and $n=32$ for DPY-27::GFP *sdc-2* RNAi. The images depict examples of intestine nuclei used for FRAP analysis. Unlike DPY-27::GFP, the ATPase EQ mutant did not show subnuclear localization, similar to when condensin DC recruiter SDC-2 was knocked down. Nuclei are outlined by white dashed lines. Scale bars: 5 μ m. (E) Co-immunoprecipitation analysis of condensin DC subunits. Protein extracts were prepared from larvae that were heat shocked for 1 h at 35°C and recovered at 20°C for 2 h or 8 h. Immunoprecipitation (IP) of condensin DC subunits DPY-27, DPY-26 and MIX-1 was performed, and immunoprecipitated DPY-27::GFP and endogenous protein were analyzed by western blotting (WB) with an anti-DPY-27 antibody. The intensity of the DPY-27::GFP and endogenous protein bands in the DPY-27 IP lane indicates the relative abundance of each protein. The intensity of DPY-27::GFP and endogenous protein bands in other lanes indicates their relative interaction with each subunit. Blots are representative of two experiments.

system in mutants and knockdown conditions to study these proteins' influence on condensin DC dynamics. In *set-1* knockdown conditions and in *set-4* null, *sir-2.1* null and *dpy-21* (*JmjC*) mutants, DPY-27 FRAP recovery was largely similar to that of wild-type animals, with a small but statistically significant reduction in mobility in the *set-4* null mutant (Fig. 4A; Fig. S4A). The most dramatic difference was observed in the *dpy-21* null

mutant (Fig. 4A). The *dpy-21* null mutant had a reduction in the percentage of mobile DPY-27::GFP from ~30% to ~10% (Fig. 4B). A control experiment bleaching DPY-27::GFP outside of the X chromosome indicated that the effect observed in the *dpy-21* null mutant was largely specific to the X chromosome (Fig. S4B). Thus, DPY-21 increases the proportion of mobile condensin DC molecules on the X chromosomes.

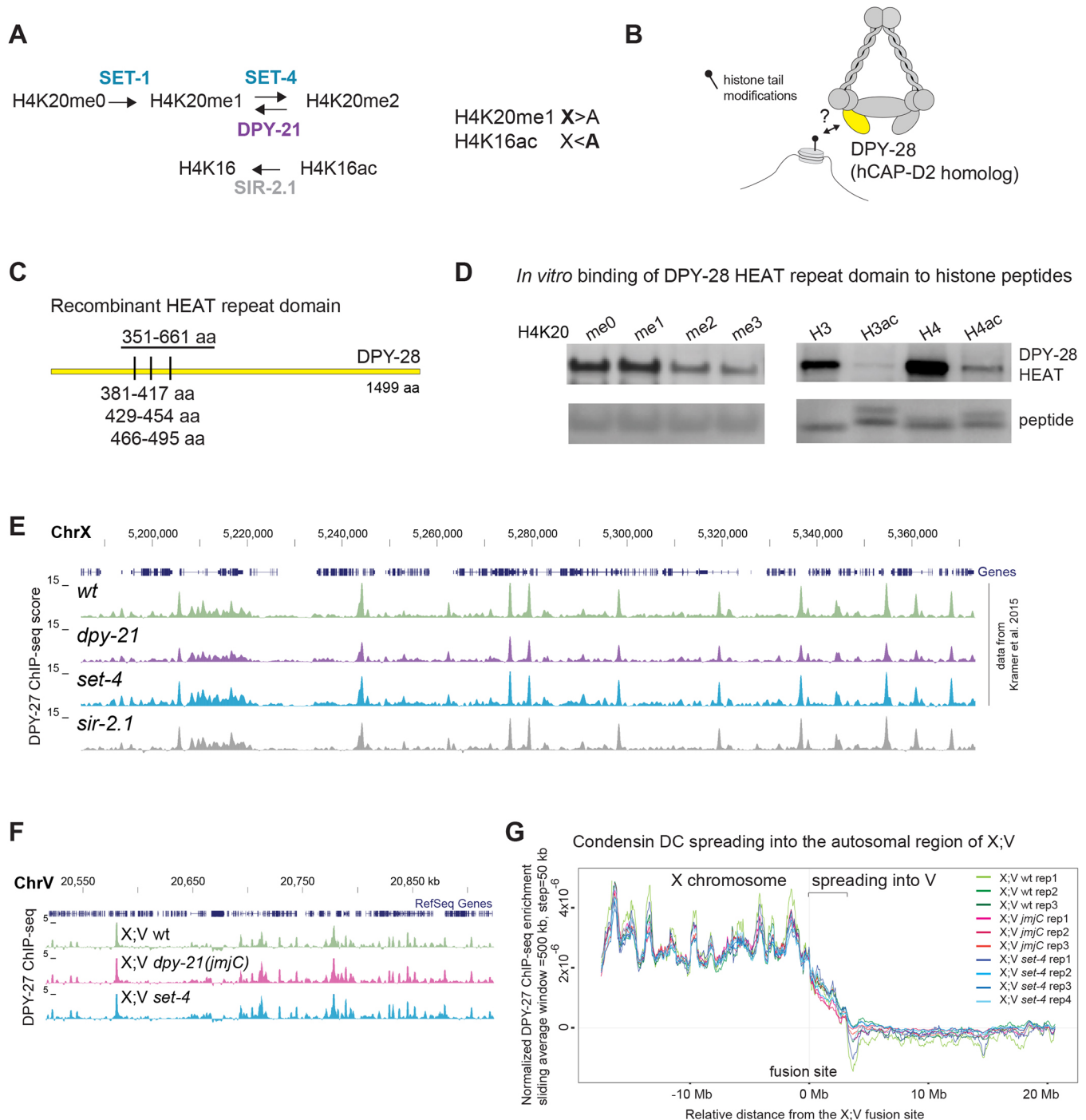


Fig. 3. See next page for legend.

Previous analysis of condensin DC localization by immunofluorescence in the *dpy-21* null mutant did not report an effect except an increase in the volume of the X chromosomes in *dpy-21* null and *dpy-21(JmjC)* mutants (Brejc et al., 2017; Lau et al., 2014). We wondered whether the reduction in mobile condensin DC produces a difference in the localization of DPY-27::Halo compared to that in wild-type cells, as determined using confocal imaging. Indeed, we noticed stronger puncta of DPY-27 signal within the X chromosomal domain in the *dpy-21* null mutant, which appears as a long tail of high pixel intensities in the distribution (Fig. 4C; Fig. S4C).

3D DNA contacts as measured by Hi-C do not change significantly in the *dpy-21* null mutant

Since *dpy-21* null mutation decreased the number of mobile condensin DC molecules as measured by FRAP, we hypothesized that DPY-21 might act similarly to the cohesin unloader WAPL (Haarhuis et al., 2017). To test this idea, we performed Hi-C analysis in *dpy-21* null embryos and repeated Hi-C in *dpy-21(JmjC)* mutants while confirming the strain (Fig. S5D) (Brejc et al., 2017). Although a subtle reduction in insulation was observed across a few *rex* sites that act as TAD boundaries, the overall TAD structure was similar to that of wild-type embryos in *dpy-21(JmjC)* and *dpy-21*

Fig. 3. Condensin DC may interact with histone tails, but *set-4*, *sir-2.1* and catalytic activity of DPY-21 do not regulate condensin DC binding as measured by ChIP-seq. (A) Enzymes that regulate H4K20 methylation and H4K16 acetylation. In hermaphrodites, H4K20me1 is increased and H4K16ac is reduced on the dosage compensated X chromosomes (X) compared to autosomes (A). The *dpy-21* null mutant is the (*e418*) allele with a premature stop codon that eliminates the protein (Yonker and Meyer, 2003), the *dpy-21(JmjC)* mutant is the (*y607*) allele, a point mutation that nearly abolishes H4K20me2 demethylase activity without eliminating the protein itself (Brejc et al., 2017). The *set-4* null mutant is (*n4600*), a knockout allele that eliminates H4K20me2 and H4K20me3 (Delaney et al., 2017). The *sir-2.1* null mutant is (*ok434*), a knockout allele that increases H4K16ac (Wells et al., 2012). (B) Cartoon depicting possible interaction of HEAT repeat-containing domain of DPY-28 (homologous to human hCAP-D2) with histone tail modifications. (C) Three HEAT repeats annotated by Pfam are shown as tick marks. The amino acids (aa) 351–661 were purified and used in peptide binding assays. (D) In-solution peptide binding assay was performed using GST-tagged DPY-28 HEAT domain and biotinylated histone N-terminal tail peptides with the indicated modifications (H3ac and H4ac indicate tetra-acetylated histone H3 and H4 peptides, respectively). The recombinant protein was incubated with peptides bound to magnetic streptavidin beads, and bound fractions were analyzed using western blot. The streptavidin signal below indicates the amount of peptide in each fraction. Methyl modified histone peptide blots representative of two replicates; acetyl and unmodified histone peptides representative of two replicates. (E) UCSC genome browser (<https://genome.ucsc.edu/>) shot of a representative region of the X chromosome (ChrX) showing similar DPY-27 ChIP-seq patterns in the *sir-2.1* null mutant. Data from wild-type N2, the *dpy-21* null mutant and the *set-4* null mutant are from Kramer et al. (2015) and are plotted for comparison. Chromosome locations are marked in kb. (F) Genome browser view of DPY-27 ChIP-seq enrichment across the fusion site on the autosomal region of the X;V chromosome in X;V wild-type, *dpy-21(JmjC)* and *set-4* null backgrounds. (G) A moving average of the DPY-27 ChIP enrichment score is plotted with a window size of 500 kb and step size of 50 kb in X;V fusion strains with wild-type, *dpy-21(JmjC)* and *set-4* null backgrounds. DPY-27 ChIP-seq data was normalized to reduce variability between replicates by z-score standardization of ChIP/input ratios to the background from autosomes I–IV, followed by equalization of total ChIP-seq signal to 1 in X;V.

null embryos on both the X chromosomes (Fig. 5A,B) and autosomes (Fig. S5A). The range of DNA interactions in the *dpy-21(JmjC)* and *dpy-21* null mutants are shown in Fig. 5C and Fig. S5B (Brejc et al., 2017).

To highlight condensin DC-mediated X chromosome-specific 3D contacts, we normalized contact frequency across the same distance on the X chromosome to autosomes. This analysis reaffirmed that, compared to autosomes, DNA contacts in the distance range of 50 kb to 1 Mb are more frequent on the X chromosomes (Fig. 5D; Fig. S5C). We reasoned that if DPY-21 protein functions as the unloader for condensin DC, a rightward shift in X chromosome-enriched contacts would be observed in the *dpy-21* null mutant as condensin DC stays loaded on DNA to form larger loops. However, the range of X chromosome-enriched contacts did not increase in both *JmjC* and null mutants of *dpy-21* (Fig. 5D). Furthermore, in contrast to stronger loops observed in the cohesin unloader WAPL mutant, interactions between *rex* sites weakened in the *dpy-21* null mutant (Fig. 5E; Fig. S5E). Thus, we conclude that DPY-21 does not act as a condensin DC unloader.

A previous analysis of the *dpy-21(JmjC)* mutant has shown a stronger effect on *rex–rex* interactions (Brejc et al., 2017). To address whether the difference between our Hi-C data and the published data in the same *dpy-21(JmjC)* mutant arises from data processing, we ran all the replicates through our analysis pipeline and compared results in several ways. The X chromosome TAD structure (Fig. S6A) and average insulation strengths across *rex* sites were stronger in our data compared to the Hi-C data from Brejc et al. (Fig. S6B). In both data sets, there was a reduction in the distance range of 3D contacts upon

dpy-21(JmjC) mutation (Fig. S6D). The X chromosome-specific reduction in the range of 3D DNA contacts was less prominent in our data (Fig. S6D). The strength of the *rex–rex* interactions (distances within Mb scale) were more variable between biological replicates and between the two sets of Hi-C experiments (Figs S5E, S6E). Whereas *rex–rex* interactions diminished in the published *dpy-21(JmjC)* mutant data (Brejc et al., 2017), they largely remained in our Hi-C data. It is not clear what underlies this difference.

The presence of stronger Hi-C interactions in our data may be due to the collection of older embryos establishing dosage compensation (Kramer et al., 2015). Alternatively, technical differences in the Hi-C protocols could be the reason. One notable technical difference is crosslinking. Brejc et al. used formaldehyde to crosslink previously frozen embryos (Brejc et al., 2017), whereas we crosslinked embryos both live before freezing and after isolating nuclei. Extensive crosslinking may have captured transient interactions in Hi-C. Consistently, compared to the data from Brejc et al. (2017), our data show more pronounced TAD structures (Fig. S6A) and X chromosome-enriched contacts (Fig. S6C,D). These features are thought to arise from the dynamic process of loop extrusion (Fudenberg et al., 2017). It is possible that the *rex–rex* interactions are differentially captured by the two crosslinking methods.

DISCUSSION

In vivo and *in vitro* studies show that SMC complex function requires ATPase activity (Hassler et al., 2018; Hirano, 2016). In *C. elegans* condensin DC, four out of five subunits are also part of the condensin I complex, thus their functional homology is apparent (Csankovszki et al., 2009). The single subunit that distinguishes condensin DC from condensin I is DPY-27, the SMC4 homolog (Csankovszki et al., 2009; Hagstrom et al., 2002). Here, we showed that a single amino acid mutation that has been shown to slow down ATP hydrolysis and impair the function of SMC4 proteins in other organisms also eliminates DPY-27 binding to the X chromosomes (Fig. 2). This observation adds to evidence that the evolutionarily conserved SMC complex activity is conserved in condensin DC (Albritton and Ercan, 2018; Lau and Csankovszki, 2014; Wood et al., 2010).

Although ATPase activity is strictly conserved, there may be differences in how different SMC complexes in different organisms are affected by ATPase mutations. In *Xenopus* extracts, incorporating the EQ mutation in SMC2 and SMC4 does not abolish loading to chromosomes, as analyzed using immunofluorescence (Kinoshita et al., 2015). Similar results have been obtained in chicken cell culture and yeast, where SMC2 and SMC4 EQ single mutants are able to bind chromosomes at levels comparable to the wild-type proteins but are not competent in chromosome compaction (Hudson et al., 2008; Thadani et al., 2018). In *Bacillus subtilis*, ChIP-seq experiments have shown that EQ-mutant SMC binds to *parS* loading sites but has reduced spreading along the chromosome (Minnen et al., 2016). Similarly, mammalian EQ-mutant cohesin binding at loading sites is less affected than at CTCF sites (Vian et al., 2018). Thus, different binding modes may have different ATPase requirements, and although the EQ mutation reduces ATP hydrolysis in all SMC complexes analyzed so far, future work is needed to characterize the specific effect of this mutation on condensin DC.

In addition to DNA loop extrusion, ATPase activity may also contribute to SMC complex formation and stability *in vivo*, perhaps by controlling the structural changes that occur through the cycle of ATP binding and hydrolysis (Lee et al., 2020). It has been reported previously that ATPase mutation has no measurable effect on complex formation in chicken cells, as measured by pull-down

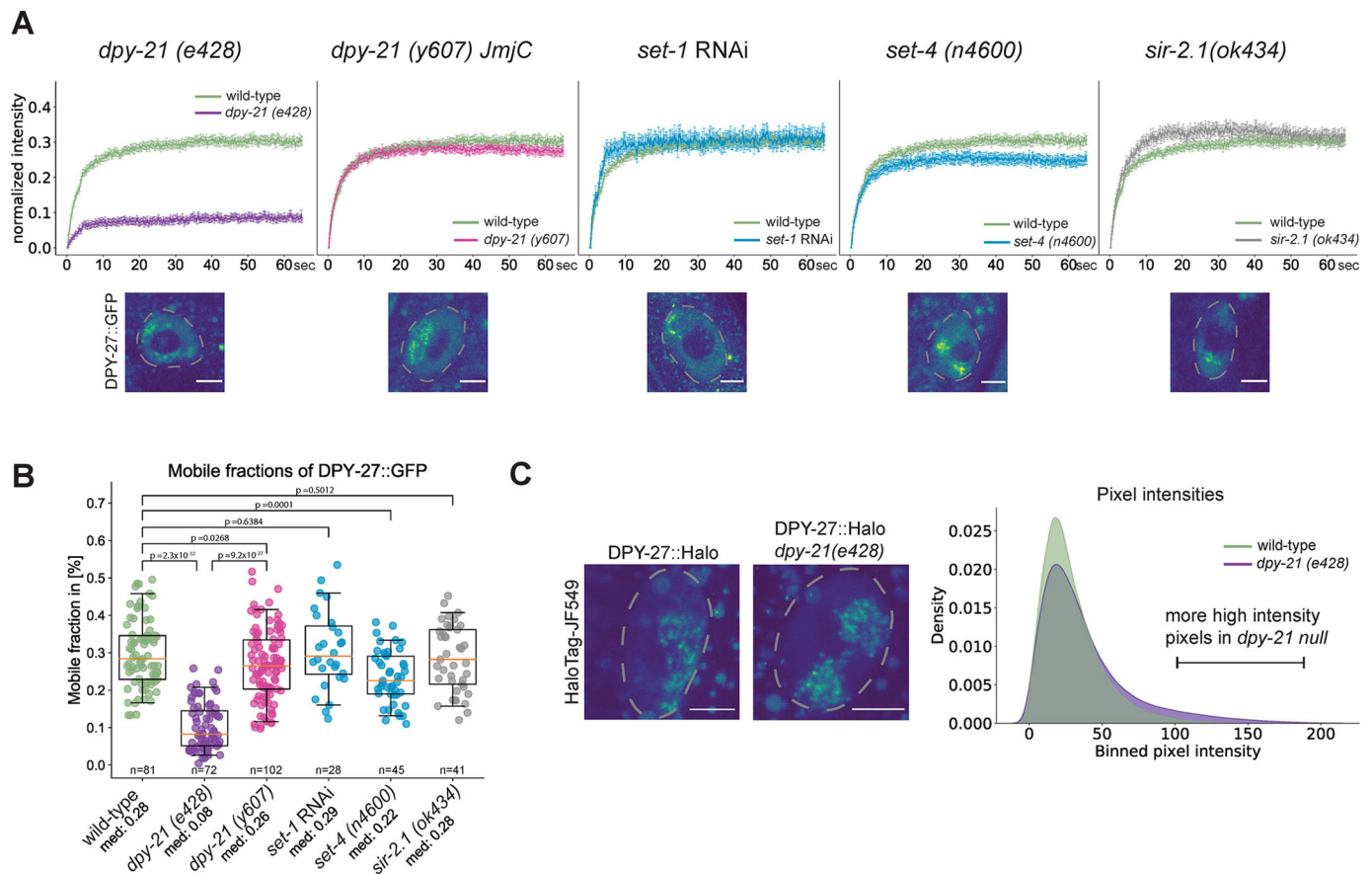


Fig. 4. The *dpy-21* null mutant but not the *dpy-21(JmjC)* catalytic mutant reduces the proportion of mobile condensin DC. (A) Mean FRAP recovery curves of DPY-27::GFP in either wild-type (green) or different mutant conditions. Data are mean±s.e.m. Numbers of bleached single intestine nuclei (from at least three biological replicates) for each experiment are *n*=81 for wild-type, *n*=72 for the *dpy-21* null mutant [*dpy-21 (e428)*], *n*=102 for the *dpy-21(JmjC)* mutant [*dpy-21 (y607)*], *n*=28 for *set-1* RNAi, *n*=45 for the *set-4* null mutant [*set-4 (n4600)*] and *n*=41 for the *sir-2.1* null mutant [*sir-2.1 (ok434)*]. Corresponding images of intestine nuclei for each mutant condition are depicted under each FRAP curve. Nuclei are outlined by dashed lines. Scale bars: 5 μ m. (B) Mobile fractions calculated from individual replicate FRAP recovery curves as shown in A. *P*-values are from a two-tailed independent two-sample *t*-test. Boxplots show the median (line), interquartile range (box). Whiskers are at the 5th and 95th percentile of the dataset. The number of images of nuclei analyzed is noted under each boxplot, along with the median values (med). (C) Analysis of endogenous DPY-27::Halo fluorescence intensity on the X chromosome in wild-type and *dpy-21* null worms. The HaloTag signal of DPY-27 was segmented in 3D and quantified in adult intestine cells in two biological replicates (Fig. S4C). The left panel depicts two example nuclei (marked by dashed lines). Scale bars: 5 μ m. For the wild-type worms, 27 images were analyzed, for the *dpy-21(e428)* mutant images of 35 nuclei were analyzed. The right panel shows the binned mean pixel fluorescence intensity for the two conditions in a smoothed density plot. The distributions of pixel intensities are significantly different in the two conditions, with a *P*-value of 1.46×10^{-114} (Mann-Whitney *U*-test).

experiments (Hudson et al., 2008), whereas in budding yeast, an ATP-binding mutation reduces the interaction between SMC4 and the kleisin subunit (Thadani et al., 2018). In *B. subtilis*, ATPase mutations reduce the SMC homodimer's proper interaction with the ScpA bridging protein, as measured by crosslinking assay (Wilhelm et al., 2015). We have also observed reduced interaction of DPY-27(EQ) with the kleisin subunit in coimmunoprecipitation experiments. These observations suggest that the ATPase cycle affects the formation of condensins *in vivo*.

Enrichment and depletion of H4K20me1 and H4K16ac on the X chromosomes have little effect on condensin DC binding measured by ChIP-seq *in vivo*

In vitro, condensin prefers to bind to free DNA (Kong et al., 2020; Kschonsak et al., 2017; Piazza et al., 2014), and *in vivo* ChIP-seq analysis of condensins in various organisms has revealed that condensins accumulate at accessible regions of the genome (Jeppsson et al., 2014; Uhlmann, 2016). Interestingly, a recent study has found that condensin is able to extrude DNA fragments

containing 3–4 nucleosomes, and that the nucleosomes increase the velocity and processivity of condensin II *in vitro* (Kong et al., 2020). In addition to nucleosomes themselves, chromatin modifications, histone variants and linker histone have been proposed to regulate condensin binding (Choppakatla et al., 2021; Kim et al., 2009; Kimura and Hirano, 2000; Liu et al., 2010; Petty et al., 2009; Tada et al., 2011; Tanaka et al., 2012; Yuen et al., 2017).

The potential for HEAT-repeat domains in CAP-D3 (also known as NCAPD3) and CAP-G2 (also known as NCAPG2) to interact with histones has been proposed for human condensin II (Liu et al., 2010). Here, we found that the recombinant HEAT-repeat domain of DPY-28 interacts with histone H3 and H4 tail peptides (Fig. 3). Yet, mutants that reduce X chromosome enrichment of H4K20me1 and increase X chromosome depletion of H4K16ac did not affect condensin DC binding as measured by ChIP-seq and showed only subtle changes in FRAP assays (Figs 3 and 4). It remains unclear whether the combined effects of multiple histone modifications, variants and linker histones on the X chromosomes regulate condensin DC binding.

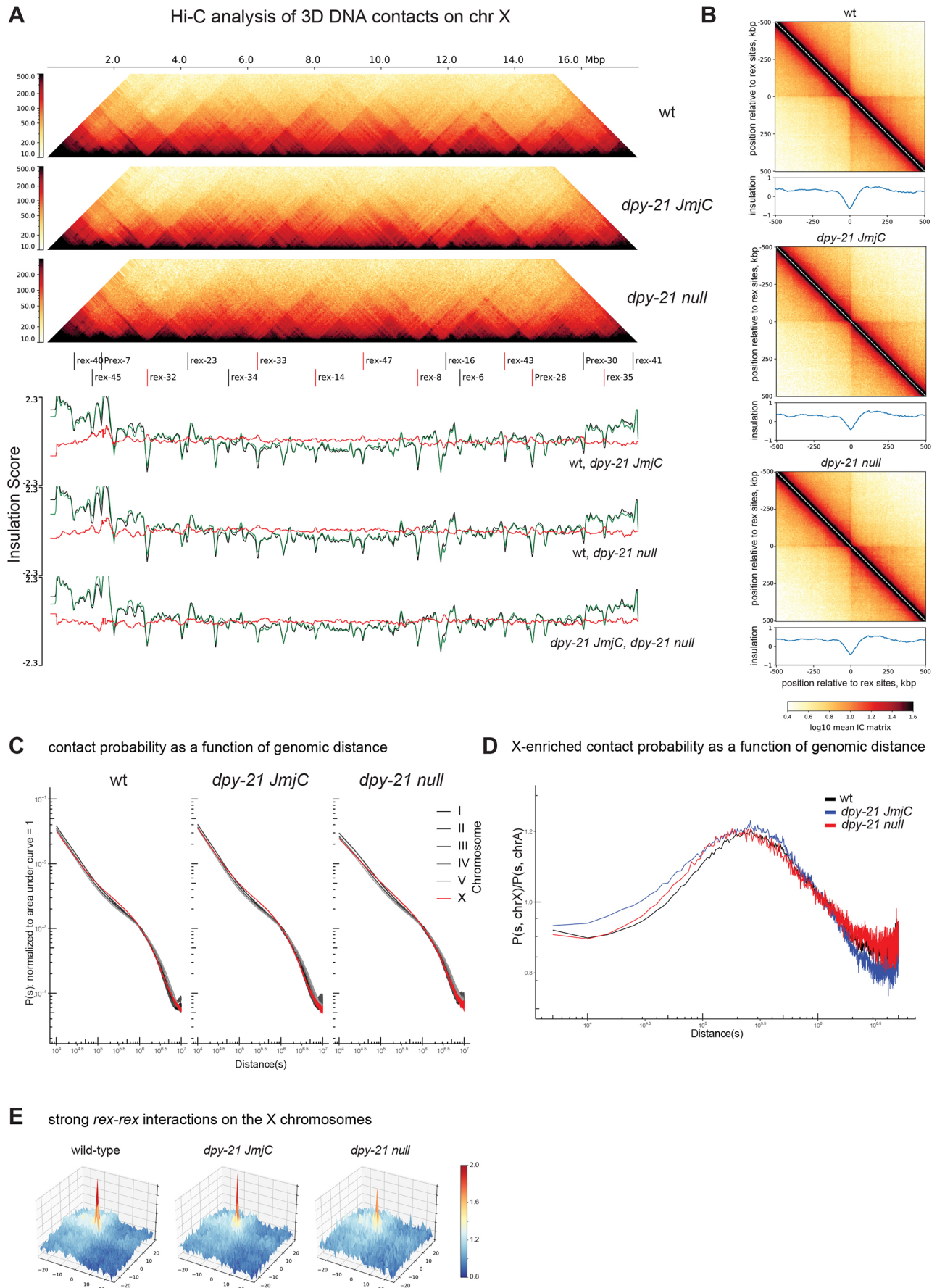


Fig. 5. See next page for legend.

Fig. 5. Hi-C analysis of 3D DNA contacts in *dpy-21(JmjC)* and *dpy-21* null mutant embryos. (A) Hi-C heatmap (top) and insulation scores (bottom) of the X chromosome (chr X) showing wild type (wt), the *dpy-21(JmjC)* mutant, and the *dpy-21* null mutant. The 'fall' colormap, adapted from cooltools, is used to depict the strength of relative contact probability between pairs of genomic bins. The 17 strong *rex* sites indicated are as annotated by Albritton et al. (2017), eight of which were annotated as DCC-dependent boundary *rex* sites (indicated by red lines) by Anderson et al. (2019). The insulation scores and their subtractions for three possible pairwise comparisons are shown in the lower panels. The insulation scores for the three pair-wise comparison are as follows: top: wild-type (black), *dpy-21(JmjC)* (green); middle wild-type (black), *dpy-21* null (green); bottom: *dpy-21(JmjC)* (black), *dpy-21* null (green); the red lines indicate per bin subtraction of green minus black. (B) Pile-up analysis showing the average Hi-C map and the insulation scores ± 500 kb surrounding the annotated 17 strong *rex* sites for the indicated genotypes. IC or 'iteratively corrected' matrix' is a type of matrix balancing used to correct for different bins having sequencing/representation bias. (C) Distance decay curve showing the relationship between 5-kb binned genomic separation, s , and average contact probability, $P(s)$ computed per chromosome for the indicated genotypes. (D) X chromosome-enriched chromosomal contacts for the indicated genotypes are visualized using an X chromosome minus autosome (X-A)-normalized distance decay curve. For every genomic separation s , the unity-normalized contact probability of the X chromosome, $P(s, \text{chrX})$, is divided by that of autosomes, $P(s, \text{chrA})$. Distances in C and D are shown in bp. (E) Meta-dot plot showing the average strength of interactions between pairs of *rex* sites on a 10 kb distance-normalized (observed divided by expected) matrix. A total of ± 25 bins (± 250 kb) regions surrounding each *rex* site are shown. For the 17 strong *rex* sites, a total of 33 *rex*-*rex* pairs located within 3 Mb of each other were used. More blue coloring indicates interaction strengths weaker than expected and more red coloring indicates strength greater than expected.

A non-catalytic activity of DPY-21 regulates the dynamics of condensin DC binding and is required for transcription repression on the X chromosomes

DPY-21 is an H4K20me2 demethylase that interacts with condensin DC and is important for dosage compensation (Brejc et al., 2017; Yonker and Meyer, 2003). Comparison of the null and catalytic *dpy-21* mutants indicates that DPY-21 plays both a structural and catalytic role in X chromosome repression (Brejc et al., 2017). The catalytic role of *dpy-21* decreases H4K20me2/3 and increases H4K20me1 on the X chromosomes and contributes to repression. Here, we showed that the non-catalytic role of DPY-21 increases the mobile fraction of condensin DC on the X chromosomes, which is critical for transcription repression.

How do the catalytic and non-catalytic activities of DPY-21 contribute to repression? DPY-21-mediated enrichment of H4K20me1 leads to reduction of H4K16ac on the X chromosomes, which may reduce binding of general activators, contributing a portion of the observed 2-fold repression provided by condensin DC (Sheikh et al., 2019). Our work suggests that a non-catalytic activity of DPY-21 contributes to repression by regulating the kinetics of condensin DC diffusion. In the *dpy-21* null mutant, but not in the *dpy-21(JmjC)* mutant, the fraction of mobile condensin DC reduced from $\sim 30\%$ to $\sim 10\%$. Interestingly, in the *dpy-21* null mutant, condensin DC binding to promoters slightly decreases (Kramer et al., 2015), and we observed that DPY-27::Halo signal showed higher intensity spots. It is possible that without DPY-21, condensin DC is more frequently 'trapped' in an immobile configuration that reduces condensin DC presence and activity at promoters that represses transcription initiation.

How does DPY-21 increase the proportion of the mobile condensin DC complexes? The results of Hi-C analysis in the *dpy-21* null mutant argue against a role akin to the cohesin unloader WAPL (Haarhuis et al., 2017; Nuebler et al., 2018). The non-catalytic activity of DPY-21 might be structural, similar to those reported for other histone-modifying enzymes, including demethylases. For example, a range of non-catalytic activities for lysine-specific

demethylase 1 (LSD1, also known as KDM1A) have been discovered, including the role of LSD1 as a scaffolding protein, destabilizing other proteins by promoting self-ubiquitylation, inhibiting autophagy, or protecting other proteins from proteasome-dependent degradation (Gu et al., 2020; Miller et al., 2020). JmjC domain-containing demethylases also show non-catalytic activities. KDM2B, an H3K36 demethylase, recruits PRC1 to unmethylated CpG islands via its zinc finger domain (He et al., 2013). Similarly, the *Drosophila* H3K36 demethylase Kdm4A regulates heterochromatin position-effect variegation independent of its catalytic activity (Colmenares et al., 2017). In fission yeast, overexpression of the histone demethylase Epe1 (also known as Jhd1) causes heterochromatin defects by recruiting the histone acetyltransferase complex SAGA, independent of the demethylase activity (Bao and Jia, 2019). For DPY-21, structural work so far has been limited to the 407 amino acids that include the JmjC domain (Brejc et al., 2017). Secondary structure prediction tools suggest that the rest of the 1641-amino-acid protein is highly unstructured. Intrinsically disordered protein domains promote protein-protein and protein-nucleic acid interactions (Davey, 2019). DPY-21 could directly or indirectly interact with condensin DC, regulate its binding to histone tails and control its mobility.

Interestingly, although X chromosomes are upregulated ~ 2 -fold in the *dpy-21* null mutant, Hi-C showed minimal change at the chromosome-wide level. This could be due to condensin DC-mediated DNA loops not being sufficient for repression or the lack of temporal or gene-level resolution of Hi-C data. Higher-resolution assays such as Micro-C may detect shorter-range DNA contacts that may be relevant to condensin-mediated repression (Swygert et al., 2019). The temporal dynamics of condensin DC may be important for repression, which could be addressed by high-resolution live imaging of condensin DC association with DNA. Here, our results suggest that the dynamics of condensin DC binding to chromatin is important for its function, and that DPY-21 regulates both histone modifications and condensin DC mobility to repress X chromosome transcription (Fig. 6).

MATERIALS AND METHODS

Strains and worm growth

A list of strains and genotypes are provided in Table S1, and primer sequences are provided in Table S2. Unless noted, worms were grown and maintained using standard methods (Stiernagle, 2006) at 20–22°C on NGM plates containing OP50-1 strain of *E. coli* as food. The worm strain *dpy-21(y607 JmjC)* was kindly provided by Barbara Meyer (University of California, Berkeley, USA).

Generation of DPY-27::GFP and DPY-27(EQ)::GFP strains

An inducible GFP-tagged copy of DPY-27 was expressed from the chromosome II Mos1-mediated single copy insertion (MosSCI) site (~ 8.4 Mb) (Frøkjær-Jensen et al., 2008) under the control of a heat-shock inducible *hsp 16-41* promoter and the *dpy-27* 3' UTR. The *hsp 16-41* promoter was amplified from pCM1.57 (Addgene plasmid #17252) using primers SE123F and SE123R, and the *dpy-27* 3' UTR was amplified from genomic DNA using primers SE124F and SE124R, and both were inserted into pCFJ151 (Addgene plasmid #19330) at the XhoI site. The resulting plasmid contained a SphI site between the promoter and the 3' UTR, which was used for NEB Infusion cloning with the full-length *dpy-27* and a GFP-3 \times flag sequence. Amplification of the *dpy-27* sequence was performed from genomic DNA using primers SE135F and SE135R. GFP-3 \times flag sequence was amplified from a plasmid kindly provided by Susan Strome (Department of Molecular, Cell, and Developmental Biology, University of California Santa Cruz, Santa Cruz, USA) using primers SE136F and SE136R. ATPase mutagenesis of DPY-27 was performed by incorporating the E-to-Q mutation at the conserved ATPase domain as shown in Fig. 2A.

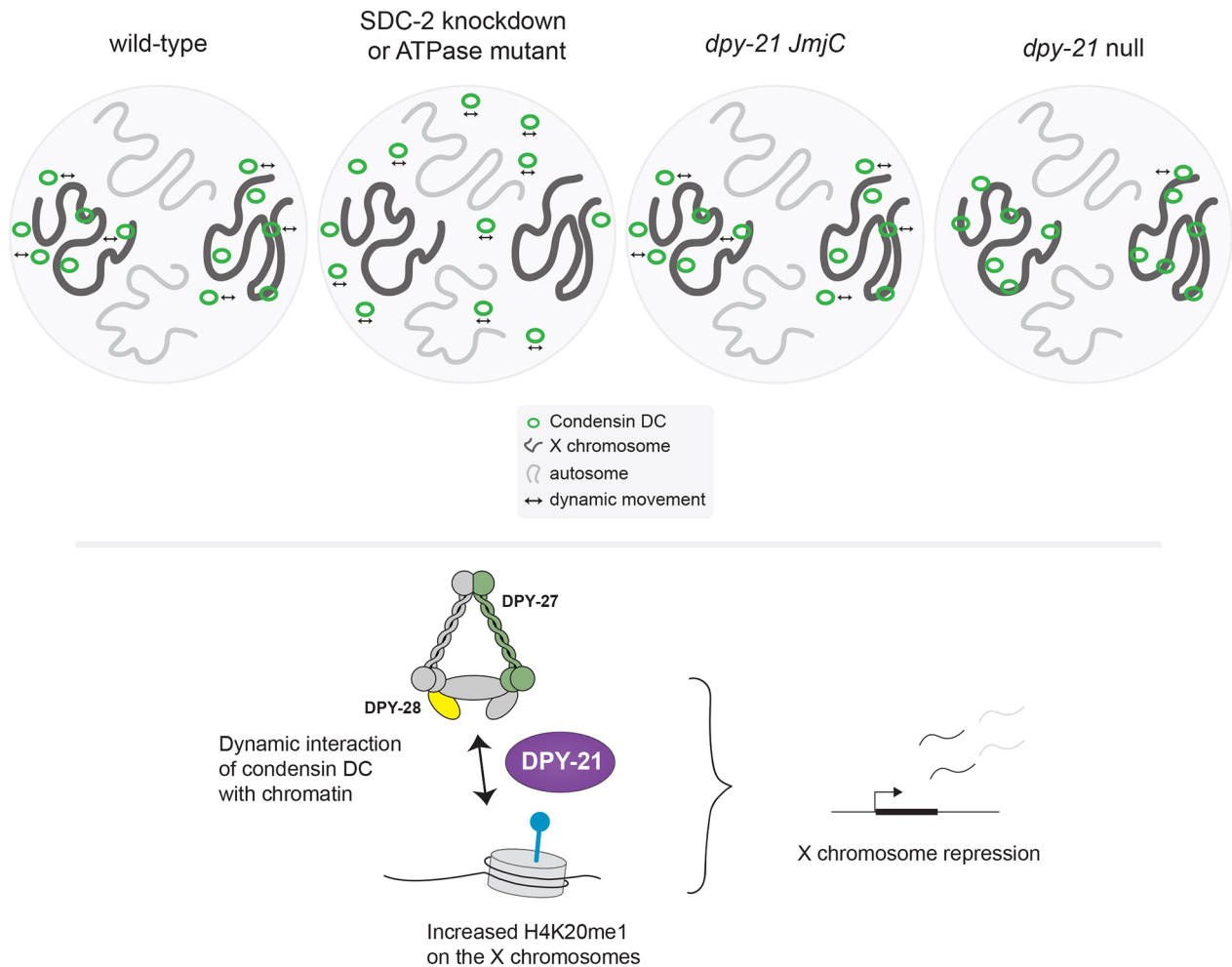


Fig. 6. Summary of results and DPY-21 function in condensin DC-mediated X chromosome repression. In a wild-type hermaphrodite cell, condensin DC binds dynamically and specifically to the X chromosomes. This binding is disrupted by knockdown of the condensing DC recruiter SDC-2 or a single amino acid mutation in the ATPase domain of DPY-27. Condensin DC may interact with histone tails through HEAT repeats within DPY-28. The H4K20me2 demethylase DPY-21 has a dual function in X chromosome repression. The catalytic activity reduces H4K20me2 and H4K20me3 and increases H4K20me1 on the X chromosome. This leads to reduced H4K16ac and contributes to repression. The non-catalytic activity of DPY-21 increases the mobility of condensin DC molecules, which is important for transcription repression. In the *dpy-21* null condition, both catalytic and non-catalytic activities are eliminated, resulting in stronger X chromosome derepression.

Generation of the DPY-27::Halo strain

The CRISPR/Cas9 system was used to insert the Halo tag at the C terminus of DPY-27 (Dokshin et al., 2018). A 20 bp crRNA (LS37) was designed to target the end of the last *dpy-27* exon. The dsDNA donors consisting of a 15 bp flexible linker (GlyGlyGlyGlySer) and the Halo tag flanked by 35 bp homology arms were generated by PCR using 5' SP9 (TEG)-modified primers AM29F and AM29R, and pLS19 (this study) as a template. The injection mix containing *Streptococcus pyogenes* Cas9 3NLS (10 µg/µl, IDT), crRNA (2 nmol, IDT), tracrRNA (5 nmol, IDT), dsDNA donors, and pCFJ90 (pharynx mCherry marker; Addgene plasmid #19327) was prepared as previously described (Dokshin et al., 2018). After injection, ~40 F1 worms that were positive for the co-injection marker were transferred to individual plates and allowed to have progeny. F2 progeny was screened by PCR with primers LS40F and LS40R. Sanger sequencing of positive PCR products showed in-frame insertion of the Halo tag along with 18 bp of unknown sequence that did not affect the function of the tagged protein (Table S5).

Generation of X;V, *set-4(n4600)* and X;V, *dpy-21(y607 JmjC)* strains

ERC57 [*set-4 (n4600) II; X;V (ypT47)*] strain was generated by crossing YPT47 with the *set-4* null deletion mutant strain MT14911. For the X;V, *dpy-21(y607 JmjC)* strain, a single amino acid substitution (H1452A),

that disrupts the demethylase activity of *dpy-21* (Brejc et al., 2017), was incorporated in the X;V (*ypT47*) strain using CRISPR/Cas9. A 200 bp single-stranded oligonucleotide repair template (BR16_oligo) was used to change the codon 1452 from CAC to GCC. The introduction of the changed codon generated a NotI restriction site that was used to screen, and the change was confirmed by Sanger sequencing (Table S6). BR17F and BR17R primers amplified a 514 bp region that encompasses the mutation site, and NotI digestion generated two fragments of 216 bp and 298 bp only in the mutated allele.

Genomic data access

The new genomic data is available at Gene Expression Omnibus (GEO) series number GSE169458, and individual accession numbers of the new and published data sets used in this study are listed in Tables S4, S7 and S8.

ChIP-seq

For the ChIP-seq analyses of GFP-tagged DPY-27 in embryos, gravid adults were heat shocked at 35°C for 30 min and transferred to room temperature for 2 h for recovery. Embryos were collected by bleaching, and ChIP was performed as described previously (Ercan et al., 2007), using 2 µg of anti-GFP (Abcam, ab290) and anti-DPY-26 antibodies with 1–2 mg of embryo extract. Detailed antibody information is given in Tables S3 and S7. The

ChIP-seq analysis of the X;V fusion strains was performed in early L3 larvae by hatching embryos in M9 buffer (Stiernagle, 2006) overnight. The next day, L1 larvae were plated on NGM medium containing HB101 *Escherichia coli* and incubated at 20°C for ~24 h. ChIP in larvae was performed by grinding frozen larvae for a few minutes in a mortar and pestle cooled using liquid nitrogen, followed by crosslinking in phosphate-buffered saline (PBS) containing 1% formaldehyde for 10 min, quenching with 125 mM glycine for 5 min, and preparing ChIP extract as in embryos. X;V wt rep2 was prepared by live crosslinking larvae. Anti-DPY-27 antibody (2 µg) was used with 1–2 mg of extract per ChIP. Half of the ChIP DNA and ~20–80 ng of the input control DNA were used to make Illumina TruSeq libraries as previously described (Albritton et al., 2017). For each data set, at least two biological replicates were generated, as listed in Table S7. Single-end sequencing was performed in Illumina HiSeq500 or NextSeq.

ChIP-seq data analysis

We used bowtie2 version 2.3.2 to align 50–75 bp single-end reads to the *C. elegans* WS220 genome with default parameters (Langmead and Salzberg, 2012). Bam sorting and indexing was performed using samtools version 2.1.1 (Ramirez-Gonzalez et al., 2012). The BamCompare tool in DeepTools version 3.3.1 was used to normalize for the sequencing depth using counts per million reads mapped (CPM) and create ChIP/input ratios with a bin size of 10 bp and 200 bp read extension (Ramirez et al., 2016). Only reads with a minimum mapping quality of 20 were used, and mitochondrial DNA, PCR duplicates and blacklisted regions were removed (Amemiya et al., 2019). The average coverage data was generated by averaging ChIP–input enrichment scores per 10 bp bins across the genome. For alignments and sliding window analysis of replicates, ChIP/input ratios were z-scored using the s.d. and mean of autosomes or chromosomes I to IV in normal and X;V karyotypes, respectively.

mRNA-seq

mRNA-seq analysis of *sir-2.1* null mutant strain VC199 (*sir-2.1*) was performed as described previously and compared to previously published mRNA-seq data (Kramer et al., 2015). Briefly, embryos and L2/L3 larvae were collected for at least three biological replicates. After collection, worms were stored in Trizol (Invitrogen). RNA was purified following the manufacturer's protocol after freeze-cracking samples five times. RNA was cleaned up using a Qiagen RNeasy kit, and mRNA was purified using Sera-Mag Oligo (dT) beads (Thermo Fisher Scientific) from 1 µg of total RNA. Stranded Illumina libraries were prepared as described previously (Kramer et al., 2015), and sequencing was performed with an Illumina HiSeq-2000 to produce single-end 50–75 bp reads. We aligned reads to the WS220 genome version using Tophat version 2.1.1 with default parameters (Kim et al., 2013). Count data was calculated using HTSeq version 0.6.1 (Anders et al., 2015) and normalized using the R package DESeq2 (Love et al., 2014). TPM counts and DESeq output files are provided in Tables S9–S14.

Hi-C

CB428 [*dpy-21(e428)*, referred to as *dpy-21* null mutant] and TY5686 [*dpy-21(y607)*, referred to as *dpy-21(JmjC)*] gravid adults were bleached to isolate embryos, which were crosslinked in 50 ml M9 containing 2% formaldehyde, washed with M9 and PBS, and pelleted at 2000 g for 1 min for storage at –80°C. Approximately 50 µl of the embryo pellet was resuspended and crosslinked a second time using the same conditions, washed once with 50 ml 100 mM Tris-HCl pH 7.5 and twice with 50 ml M9. The embryo pellet was resuspended in 1 ml embryo buffer (110 mM NaCl, 40 mM KCl, 2 mM CaCl₂, 2 mM MgCl₂, 25 mM HEPES-KOH pH 7.5) containing 1 unit of chitinase (Sigma) and then digested for ~15 min. Blastomeres were then washed with embryo buffer twice by spinning at 1000 g for 5 min. The pellet was resuspended in 1 ml Nuclei Buffer A (15 mM Tris-HCl pH 7.5, 2 mM MgCl₂, 0.34 M sucrose, 0.15 mM spermine, 0.5 mM spermidine, 1 mM DTT, 0.5 mM PMSF, 1×Calbiochem Protease Inhibitor cocktail I, 0.25% NP-40 and 0.1% Triton X-100), centrifuged at 1000 g for 5 min at 4°C then resuspended in 1.5 ml Nuclei Buffer A. The embryos were Dounce homogenized ten times with a loose pestle A and ten times with a tight pestle B. The cellular debris was spun down for 1 min at 200 g. The supernatant containing nuclei was kept on ice.

The pellet was resuspended in 1.5 ml Nuclei Buffer A, and the Dounce homogenization process was repeated four times. Each supernatant was checked for absence of debris by DAPI staining, and supernatants were pooled and spun down at 1000 g for 10 mins at 4°C. Next, ~20 µl of nuclei was used to proceed to the Arima Hi-C kit, which uses two 4-base cutters, DpnII (G^ATGC) and HinfI (G^ANTC), followed by a KAPA Hyper Prep Kit for library preparation per the protocol provided by Arima. Paired-end Illumina sequencing was performed with Nextseq or Novaseq.

Hi-C data analysis

Reads of 150 bp were trimmed using fastx toolkit version 0.0.14 (http://hannonlab.cshl.edu/fastx_toolkit/index.html) to match replicates generated by 100-bp paired-end sequencing. The Hi-C data was mapped to ce10 (WS220) reference genome using default parameters of the Juicer pipeline version 1.5.7 (Durand et al., 2016). Because Hi-C data generated from the Arima Hi-C kit used two restriction enzymes, dpnII (G^ATGC) and hinfI (G^ANTC), whereas the published Hi-C data used only one, dpnII (G^ATGC), the corresponding restriction site files were used for the juicer pipeline. The mapping statistics from the inter_30.txt output file are provided in Table S8. The inter_30.hic outputs were converted to h5 using the hicConvertFormat of HiCExplorer version 3.5.1 for genome-wide normalization and sample-to-sample depth normalization (Ramirez et al., 2018; Wolff et al., 2018, 2020). The inter_30.hic files were first converted to cool files, and the correction method was removed using the –correction_name none option. Then, cool files were converted to h5 files to be used in HiCExplorer as follows. The replicates of the same experimental condition were combined using hicSumMatrices. The count values of each replicate were normalized to match those of the most shallow matrix using hicNormalize with the option –smallest. The same method was used for the summed matrices. Lastly, the hicCorrectMatrix function was applied to each matrix to correct for sequencing bias with the following parameters: –correction_method ICE, –t 1.7 5, –skipDiagonal, –chromosomes I II III IV V X. The distance decay curves were generated by computing the average contact for a given distance using the 5000 bp-binned normalized matrix using hicPlotDistVsCounts with parameters –perchr, maxdepth 20,000,000. The outputs from –outFileData were plotted in R. The curves were normalized to unity to compare different samples by setting the sum of contacts in the distance range of 5000 bp–4 Mb to 1 for each chromosome. To analyze X chromosome-specific changes, we calculated $P(s,chrX)/P(s,chrA)$ by dividing the $P(s)$ of the X chromosome by the average $P(s)$ of all autosomes (chrA) at every distance, s . The insulation scores were computed using the 10kb-binned normalized matrix with the function hicFindTADs using parameters: –correctForMultipleTesting fdr, –minDepth 80,000, –maxDepth 200,000, –step 40,000. The meta-loops were computed using the 10 kb-binned normalized matrix with the hicAggregateContacts function of hicexplorer with parameters: –range 100,000:3,000,000, –avgType mean, –transform obs/exp, –plotType 3d, –vMin 0.8 –vMax 2 –BED 17 strong *rexes* (Albritton et al., 2017). A 400 bp window for the 17 strong *rex* sites defined in Albritton et al. (2017) was used as center regions with an additional 250 kb up- and down-stream regions. The pileup analysis at *rex* sites was done using cooltools (<https://github.com/open2c/cooltools>) by converting the corrected matrix from hicexplorer format to cool format using hicConvertFormat function.

Immunoprecipitation and western blots

Immunoprecipitations of GFP-tagged DPY-27 proteins were performed from protein extracts prepared using 200 µl of young adult worms heat shocked at 35°C for 1 h and allowed to recover at 20°C for the indicated times. For immunoprecipitation from embryos, heat-shocked adults were bleached after recovery to obtain ~100 µl embryos. Worms were Dounce homogenized in lysis buffer (40 mM HEPES pH 7.5, 10% glycerol, 150 mM NaCl, 1 mM EDTA and 0.5% NP-40) complemented with protease inhibitors (Calbiochem cocktail I) and sonicated for 5 min (30 s on and 30 s off in a Bioruptor). Extracts were centrifuged at 17,000 g for 15 min at 4°C, and 2 mg of protein was incubated overnight with 2–3 µg of the indicated antibody. Antibody details are provided in Table S3. Immunocomplexes were collected with Protein A Sepharose beads (Cytiva, 7-5280-01) at 4°C

for 2 h. Beads were washed thrice with 1 ml of immunoprecipitation buffer (50 mM HEPES-KOH pH 7.6, 1 mM EDTA, 0.05% Igepal and 150 mM NaCl). Immunoprecipitated proteins were eluted by boiling in SDS sample buffer and were analyzed by SDS-PAGE and immunoblotting using an anti-DPY-27 antibody (1:2000). Detection was performed using ECL Plus reagents (#PI80196, Thermo Fisher Scientific).

Worm size analysis

Quantification of worm size was performed in the young adult stage. Worms were allowed to lay eggs for 4 h, and the progeny were grown at 20°C to a young adult stage. Worms were washed with M9, anesthetized with 10 mM levamisole, and placed on a fresh NGM plate without OP50 to achieve an even and clear background. Single worms were obtained using an eyelash, and images of ~30 worms were acquired using a Dino-Lite eyepiece camera (AM7025X) on a Zeiss stereomicroscope with a 1× magnification. For analysis, the background was subtracted using Fiji (Schindelin et al., 2012) with a rolling ball radius of 50 pixels (light background). The Fiji plugin WormSizer (Moore et al., 2013) was used to analyze worm size and width, and plots were created using Python (https://github.com/ercanlab/2021_Breimann_et_al).

RNAi conditions

For RNAi experiments, bacterial strains from the Ahringer RNAi library (Fraser et al., 2000) were verified by Sanger sequencing and used for knockdown experiments (*set-1* and *sdc-2*, as well as *pop-1*, which acted as control for efficiency of the RNAi plates) and empty vector (negative control). Single colonies of bacteria were picked and grown in 10 ml LB medium with 50 µg/ml ampicillin overnight (at 37°C shaking at 300 rpm), then transferred to a 400 ml LB with 50 µg/ml ampicillin culture. After 2 h, when the culture reached OD ~1, expression was induced with 0.1 mM IPTG and cultures were grown for another 3 h. Bacteria were concentrated 10-fold and seeded onto 10 cm NGM plates supplemented with 50 µg/ml ampicillin, 2 µg/ml tetracycline and 1 mM IPTG. Worms were synchronized by bleaching, and L1 larvae were placed on the seeded plates. Worms were used for FRAP experiments after 72 h at 20°C (young adult stage). FRAP experiments for the *set-1* RNAi condition were performed in germline-less worms, indicating successful protein knockdown (Vielle et al., 2012).

Heat shock, fluorescent labeling and mounting worms for imaging

JF549-HaloTag and JF635-HaloTag ligands were a generous gift from Luke D. Lavis and Jonathan B. Grimm (Janelia Research Farm, Ashburn, USA; Grimm et al., 2015, 2017), and were incorporated into worms by feeding based on a previously reported protocol (Wu et al., 2019) with the following modifications. L4 worms were washed and collected in small Eppendorf tubes with 200 µl M9, concentrated OP50 and 2.5 µM HaloTag dye. Tubes were rotated at room temperature for about 17 h, and worms were then placed on fresh OP50 plates for at least 4 h to reduce the background signal of the unbound HaloTag ligand.

For imaging experiments using the heat shock-inducible DPY-27::GFP, worms were grown to young adult stage and heat shocked for 1 h at 35°C before being recovered at room temperature for 8 h (unless otherwise labeled). Worms were settled in M9 at 4°C for 10 min, and 40 µl was transferred to a well-depression microscopy slide with the addition of 10 µl of 50 mM levamisole (LGC). After 10 min, the worms were transferred onto a 10% agarose pad on a microscope slide and covered with a 1.7 µm objective slide (high precision, no.1.5H, Marienfeld). Excess liquid was removed using a lab tissue (Kimtech precision wipe), and the edges of the objective slide were sealed with a two-component silicone glue (picodent twinsil speed).

Confocal microscopy and FRAP

Confocal imaging and FRAP were performed on a scanning confocal microscope (Leica SP8) using an HC PL APO 63×1.3 NA glycerol objective (Leica) and Leica Application Suite X (version 3.5.5.19976). For GFP, the white-light laser was set to 482 nm with 10–15% laser intensity, and the emission detection was set to 488–520 nm with a HyD hybrid photodetector and gain of 162%. For JF549, the white-light laser was set to 549 nm with

10% laser intensity, and the emission detection was set to 554–651 nm with a HyD detector and gain of 200% and gating between 0.3 and 6.0. For JF635, the white-light laser was set to 633 nm with 10% laser intensity, and the emission detection was set to 638–777 nm with a HyD detector and gain of 100% and gating between 0.3 and 6.0.

For FRAP in the intestine nuclei, 20 pre-bleach images were acquired, followed by a point bleach (smallest possible bleach spot) of 700 ms with 100% laser power and subsequent acquisition of ~500 recovery images using 10–15% laser power. The scan speed was set to 600 Hz, with bidirectional scanning (phase X, 29.752) in a frame size of 256×256 pixels (pixel dwell time 0.002425 s). The pinhole was set to 1 AU, and a 7× digital zoom was used to zoom in to single intestine nuclei of young adult worms. The FRAP experimental protocol can be found here: <https://dx.doi.org/10.17504/protocols.io.bpkymkxw>.

FRAP data analysis

Image analysis of the fluorescence recovery at the bleach point was performed using a custom-written script in MATLAB (MathWorks). First, lateral drift in pre- and post-bleach image stacks was corrected using discrete Fourier transforms (DFT)-based sub-pixel image registration (Guizar-Sicairos et al., 2008). The area of each intestine nucleus was then manually segmented. The bleached region was determined by automated thresholding (Otsu's method) of an image of the difference of the mean pre-bleach images and the mean of the first five post-bleach images. Acquisition bleaching was detected in the mean intensity of the whole nucleus region of interest in the post-bleach images. This decrease in intensity was fitted with a monoexponential decay and used to correct the acquisition bleaching during fluorescence recovery. To correct for differences in initial intensity and extent of photobleaching, such that different data sets could be directly compared, each acquisition-bleaching-corrected curve was then normalized to an initial value of 1 and an immediate post-bleach value of 0. To estimate the fraction of fluorescent proteins that can diffuse into the bleached region during the experiment's time course (mobile fraction) and the recovery time constant (τ), the post-bleach recovery was fitted with monoexponential function with nonlinear least-squares-based fitting. The mobile fraction was calculated from the monoexponential fit at each experiment's last recorded recovery time point. The recovery half time ($T_{1/2}$), corresponding to the time required to recover half of the fluorescence maximum, is estimated directly from the data. The mean normalized relative intensity of all repeats for each experimental condition was calculated and plotted for each time point with the s.e.m. using Python. The MATLAB analysis script can be found here: https://github.com/ercanlab/2021_Breimann_et_al.

Intensity distribution analysis

To compare the protein expression and X chromosome-enrichment of DPY-27::GFP and DPY-27(EQ)::GFP, images were recorded at 3 h and 8 h after a 1 h heat shock at 35°C. Two-dimensional images were manually segmented for the nuclear region, and pixel intensity values for the GFP-tagged proteins were recorded for at least 20 images per condition. To compare the average density of pixel intensities per condition, the pixel intensities were binned to ranges of 20, summed for all images of one condition, and divided by the number of used images using Python.

To compare image intensities of endogenous DPY-27::Halo in wild-type and *dpy-21* null conditions, worms were stained with HaloTag-JF549, as described above, and z-stack images were recorded to capture the complete intestinal nuclei. To compare DPY-27::Halo enrichment at the X chromosome between different conditions, the HaloTag signal was segmented in 3D using autocontext pixel classification in ilastik, resulting in a simple segmentation that assigns the most probable class for each pixel (Berg et al., 2019). Using Fiji (Schindelin et al., 2012), a binary 3D mask was created from the ilastik segmentation using Otsu's method and used to segment the HaloTag signal. Binned pixel intensities were recorded from both conditions, and density plots were created using Python (https://github.com/ercanlab/2021_Breimann_et_al).

Recombinant protein and peptide binding assay

The DNA encoding amino acids 351–661 of the DPY-28 protein was amplified from cDNA using the primers DPY 28 351F and DPY-28 660R

(Table S2). The cDNA template was prepared from total RNA using SuperScript III (Invitrogen) according to the manufacturer's protocol. The PCR product was digested with BamHI and EcoRI, and was cloned into corresponding sites in pGEX-5X-2 (GE Healthcare). The plasmid was transformed to a BL21 codon+ *E. coli* strain to be induced with 1 mM IPTG for 3 h at 25°C and purified using standard GST protein purification using GE Healthcare Glutathione Sepharose 4B, based on the manufacturer's protocol, and the protein amount was quantified using a Bradford assay. The peptides were kindly provided by Brian Strahl (UNC Biochemistry and Biophysics, Chapel Hill, USA) (Fig. S3D). Briefly, 60 µl of magnetic streptavidin beads (Dynabeads M280; Invitrogen) were washed twice with 1 ml recombinant protein binding buffer (rPBB; 50 mM Tris-HCl pH 8, 0.3 M NaCl, 0.1% Igepal CA360) and incubated rotating for 1 h with 1 nmol peptide at 4°C. The beads were washed twice with rPBB and incubated with 40 pmol of recombinant protein for 3 h, rotating at 4°C. The beads were washed 5 min thrice with rPBB and resuspended in 30 µl SDS sample buffer, and 15 µl was run on a 4–12% Bis-Tris MOPS gel (Invitrogen), transferred to a PVDF membrane and blocked with 1×PBS containing 0.1% Tween-20 and 5% dry milk. Bound peptides were visualized using an anti-GST antibody (GE 27-4577-50; 1:2000) and HRP-conjugated donkey anti-goat-IgG antibody (Promega V8051; 1:10,000) with ECL Plus (GE) and a Typhoon scanner.

Acknowledgements

We thank Barbara Meyer for the *dpy-21 (JmjC)* strain, Brian Strahl and Scott Rothbart for peptides and the in-solution peptide binding protocol, and Luke Lavis and Jonathan Grimm for the HaloTag dyes. We thank Lennon Matchett-Oates, Parvathy Manoj, Mandy Terne and Lara Winterkorn for their contributions to the project in general, and Ibai Irastorza Azcarate and Gesa Loof for help with data visualization. We thank the sequencing and imaging facilities at the NYU Biology and the Center for Genomics and Systems Biology, and the Berlin Institute for Medical Systems Biology (BIMSB). We thank the MDC–NYU PhD exchange program for enabling this collaboration.

Competing interests

The authors declare no competing or financial interests.

Author contributions

Conceptualization: L.B., A.K.M., J.K., S.E.; Methodology: L.B., A.K.M., J.K.; Software: L.B., E.B., A.W.; Validation: L.B.; Formal analysis: L.B., A.K.M., J.K., D.S.J.; Investigation: L.B., A.K.M., J.K., D.S.J., N.M., K.B., M.J.C., K.C., V.-F.S., S.E.A., M.K., L.A.S., S.P., A.W., S.E.; Resources: S.P., A.W.; Data curation: L.B., A.K.M., J.K.; Writing - original draft: L.B., A.K.M., S.E.; Writing - review & editing: L.B., A.K.M., J.K., S.E.; Visualization: L.B., A.K.M., J.K., D.S.J.; Supervision: S.P., A.W., S.E.; Project administration: S.P., S.E.; Funding acquisition: S.P., S.E.

Funding

This work was supported by the National Institute of General Medical Sciences of the National Institutes of Health (award numbers R01 GM107293 and R35 GM130311 to S.E.). L.B. was supported in part by the Joachim Herz Stiftung (#850022), and D.S.J. was supported in part by a National Institute of General Medical Sciences Predoctoral Fellowship (T32HD007520). Deposited in PMC for immediate release.

Data availability

Our new genomic data are available at Gene Expression Omnibus (GEO) as gene expression data series GSE169458, and individual accession numbers of the new and published data sets used in this study are listed in Tables S4, S7 and S8.

Peer review history

The peer review history is available online at <https://journals.biologists.com/jcs/article-lookup/doi/10.1242/jcs.258818>.

References

Albritton, S. E. and Ercan, S. (2018). Caenorhabditis elegans dosage compensation: insights into condensin-mediated gene regulation. *Trends Genet.* **34**, 41–53. doi:10.1016/j.tig.2017.09.010

Albritton, S. E., Kranz, A.-L., Winterkorn, L. H., Street, L. A. and Ercan, S. (2017). Cooperation between a hierarchical set of recruitment sites targets the X chromosome for dosage compensation. *eLife* **6**, e23629–e23645. doi:10.7554/eLife.23645

Amemiya, H. M., Kundaje, A. and Boyle, A. P. (2019). The ENCODE blacklist: identification of problematic regions of the genome. *Sci. Rep.* **9**, 9354. doi:10.1038/s41598-019-45839-z

Anders, S., Pyl, P. T. and Huber, W. (2015). HTSeq—a Python framework to work with high-throughput sequencing data. *Bioinformatics* **31**, 166–169. doi:10.1093/bioinformatics/btu638

Anderson, E. C., Frankino, P. A., Higuchi-Sanabria, R., Yang, Q., Bian, Q., Podshivalova, K., Shin, A., Kenyon, C., Dillin, A. and Meyer, B. J. (2019). X Chromosome domain architecture regulates caenorhabditis elegans lifespan but not dosage compensation. *Dev. Cell* **51**, 192–207.e6. doi:10.1016/j.devcel.2019.08.004

Bao, K. and Jia, S. (2019). Noncatalytic function of a JmjC domain protein disrupts heterochromatin. *Epigenetics Insights* **12**, 2516865719862249. doi:10.1177/2516865719862249

Berg, S., Kutra, D., Kroeger, T., Straehle, C. N., Kausler, B. X., Haubold, C., Schiegg, M., Ales, J., Beier, T., Rudy, M. et al. (2019). ilastik: interactive machine learning for (bio)image analysis. *Nat. Methods* **16**, 1226–1232. doi:10.1038/s41592-019-0582-9

Brejč, K., Bian, Q., Uzawa, S., Wheeler, B. S., Anderson, E. C., King, D. S., Kranzusch, P. J., Preston, C. G. and Meyer, B. J. (2017). Dynamic control of X chromosome conformation and repression by a histone H4K20 demethylase. *Cell* **171**, 85–102.e23. doi:10.1016/j.cell.2017.07.041

Cacciari, A. S. and Rowland, B. D. (2019). Loop formation by SMC complexes: turning heads, bending elbows, and fixed anchors. *Curr. Opin. Genet. Dev.* **55**, 11–18. doi:10.1016/j.gde.2019.04.010

Chao, L. F.-I., Singh, M., Thompson, J., Yates, J. R. and Hagstrom, K. A. (2017). An SMC-like protein binds and regulates Caenorhabditis elegans condensins. *PLoS Genet.* **13**, e1006614. doi:10.1371/journal.pgen.1006614

Choppakatti, P., Dekker, B., Cutts, E. E., Vannini, A., Dekker, J. and Funabiki, H. (2021). Linker histone H1.8 inhibits chromatin-binding of condensins and DNA topoisomerase II to tune chromosome length and individualization. *Elife* **10**, e68918. doi:10.7554/eLife.68918

Colmenares, S. U., Swenson, J. M., Langley, S. A., Kennedy, C., Costes, S. V. and Karpen, G. H. (2017). Drosophila histone demethylase KDM4A has enzymatic and non-enzymatic roles in controlling heterochromatin integrity. *Dev. Cell* **42**, 156–169.e5. doi:10.1016/j.devcel.2017.06.014

Crane, E., Bian, Q., McCord, R. P., Lajoie, B. R., Wheeler, B. S., Ralston, E. J., Uzawa, S., Dekker, J. and Meyer, B. J. (2015). Condensin-driven remodelling of X chromosome topology during dosage compensation. *Nature* **523**, 240–244. doi:10.1038/nature14450

Csankovszki, G., McDonel, P. and Meyer, B. J. (2004). Recruitment and spreading of the C. elegans dosage compensation complex along X chromosomes. *Science* **303**, 1182–1185. doi:10.1126/science.1092938

Csankovszki, G., Collette, K., Spahl, K., Carey, J., Snyder, M., Petty, E., Patel, U., Tabuchi, T., Liu, H., McLeod, I. et al. (2009). Three distinct condensin complexes control C. elegans chromosome dynamics. *Curr. Biol.* **19**, 9–19. doi:10.1016/j.cub.2008.12.006

Davey, N. E. (2019). The functional importance of structure in unstructured protein regions. *Curr. Opin. Struct. Biol.* **56**, 155–163. doi:10.1016/j.sbi.2019.03.009

Delaney, C. E., Chen, A. T., Graniel, J. V., Dumas, K. J. and Hu, P. J. (2017). A histone H4 lysine 20 methyltransferase couples environmental cues to sensory neuron control of developmental plasticity. *Development* **144**, dev.145722. doi:10.1242/dev.145722

Dokshin, G. A., Ghanta, K. S., Piscopo, K. M. and Mello, C. C. (2018). Robust genome editing with short single-stranded and long, partially single-stranded DNA donors in Caenorhabditis elegans. *Genetics* **210**, 781–787. doi:10.1534/genetics.118.301532

Durand, N. C., Shamim, M. S., Machol, I., Rao, S. S. P., Huntley, M. H., Lander, E. S. and Aiden, E. L. (2016). Juicebox provides a one-click system for analyzing loop-resolution Hi-C experiments. *Cell Syst.* **3**, 95–98. doi:10.1016/j.cels.2016.07.002

Ercan, S., Giresi, P. G., Whittle, C. M., Zhang, X., Green, R. D. and Lieb, J. D. (2007). X chromosome repression by localization of the C. elegans dosage compensation machinery to sites of transcription initiation. *Nat. Genet.* **39**, 403–408. doi:10.1038/ng1983

Ercan, S., Dick, L. L. and Lieb, J. D. (2009). The C. elegans dosage compensation complex propagates dynamically and independently of X chromosome sequence. *Curr. Biol.* **19**, 1777–1787. doi:10.1016/j.cub.2009.09.047

Fraser, A., Kamath, R.K., Zipperlen, P., Martinez-Campos, M., Sohrmann, M. and Ahringer, J. (2000). Functional genomic analysis of C. elegans chromosome I by systematic RNA interference. *Nature* **408**, 325–330. doi:10.1038/35042517

Frøkjær-Jensen, C., Davis, M. W., Hopkins, C. E., Newman, B. J., Thummel, J. M., Olesen, S.-P., Grunnet, M. and Jørgensen, E. M. (2008). Single-copy insertion of transgenes in Caenorhabditis elegans. *Nat. Genet.* **40**, 1375–1383. doi:10.1038/ng.248

Fudenberg, G., Abdennur, N., Imakaev, M., Goloborodko, A. and Mirny, L. A. (2017). Emerging evidence of chromosome folding by loop extrusion. *Cold Spring Harbor Symp. Quant. Biol.* **82**, 45–55. doi:10.1101/sqb.2017.82.034710

Gerlich, D., Hirota, T., Koch, B., Peters, J.-M. and Ellenberg, J. (2006). Condensin I stabilizes chromosomes mechanically through a dynamic interaction in live cells. *Curr. Biol.* **16**, 333–344. doi:10.1016/j.cub.2005.12.040

- Goloborodko, A., Marko, J. F. and Mirny, L. A.** (2016). Chromosome compaction by active loop extrusion. *Biophys. J.* **110**, 2162–2168. doi:10.1016/j.bpj.2016.02.041
- Grimm, J. B., English, B. P., Chen, J., Slaughter, J. P., Zhang, Z., Revyakin, A., Patel, R., Macklin, J. J., Normanno, D., Singer, R. H. et al.** (2015). A general method to improve fluorophores for live-cell and single-molecule microscopy. *Nat. Methods* **12**, 244–250. doi:10.1038/nmeth.3256
- Grimm, J. B., Muthusamy, A. K., Liang, Y., Brown, T. A., Lemon, W. C., Patel, R., Lu, R., Macklin, J. J., Keller, P. J., Ji, N. et al.** (2017). A general method to fine-tune fluorophores for live-cell and in vivo imaging. *Nat. Methods* **14**, 987–994. doi:10.1038/nmeth.4403
- Gu, F., Lin, Y., Wang, Z., Wu, X., Ye, Z., Wang, Y. and Lan, H.** (2020). Biological roles of LSD1 beyond its demethylase activity. *Cell. Mol. Life Sci.* **77**, 3341–3350. doi:10.1007/s00018-020-03489-9
- Guizar-Sicairos, M., Thurman, S. T. and Fienup, J. R.** (2008). Efficient subpixel image registration algorithms. *Opt. Lett.* **33**, 156. doi:10.1364/OL.33.000156
- Haarhuis, J. H. I., van der Weide, R. H., Blomen, V. A., Yáñez-Cuna, J. O., Amendola, M., van Ruiten, M. S., Krigger, P. H. L., Teunissen, H. et al.** (2017). The cohesin release factor WAPL restricts chromatin loop extension. *Cell* **169**, 693–700.e14. doi:10.1016/j.cell.2017.04.013
- Hagstrom, K. A., Holmes, V. F., Cozzarelli, N. R. and Meyer, B. J.** (2002). *C. elegans* condensin promotes mitotic chromosome architecture, centromere organization, and sister chromatid segregation during mitosis and meiosis. *Genes Dev.* **16**, 729–742. doi:10.1101/gad.968302
- Hassler, M., Shaltiel, I. A. and Haering, C. H.** (2018). Towards a unified model of SMC complex function. *Curr. Biol.* **28**, R1266–R1281. doi:10.1016/j.cub.2018.08.034
- He, J., Shen, L., Wan, M., Taranova, O., Wu, H. and Zhang, Y.** (2013). Kdm2b maintains murine embryonic stem cell status by recruiting PRC1 complex to CpG islands of developmental genes. *Nat. Cell Biol.* **15**, 373–384. doi:10.1038/ncb2702
- Hirano, T.** (2016). Condensin-based chromosome organization from bacteria to vertebrates. *Cell* **164**, 847–857. doi:10.1016/j.cell.2016.01.033
- Hirano, M. and Hirano, T.** (2004). Positive and negative regulation of SMC-DNA interactions by ATP and accessory proteins. *EMBO J.* **23**, 2664–2673. doi:10.1038/sj.emboj.7600264
- Hudson, D. F., Ohta, S., Freisinger, T., Macisaac, F., Sennels, L., Alves, F., Lai, F., Kerr, A., Rappsilber, J. and Earnshaw, W. C.** (2008). Molecular and genetic analysis of condensin function in vertebrate cells. *Mol. Biol. Cell* **19**, 3070–3079. doi:10.1091/mbc.e08-01-0057
- Jans, J., Gladden, J. M., Ralston, E. J., Pickle, C. S., Michel, A. H., Pferdehirt, R. R., Eisen, M. B. and Meyer, B. J.** (2009). A condensin-like dosage compensation complex acts at a distance to control expression throughout the genome. *Genes Dev.* **23**, 602–618. doi:10.1101/gad.1751109
- Jeppsson, K., Carlborg, K. K., Nakato, R., Berta, D. G., Lilienthal, I., Kanno, T., Lindqvist, A., Brink, M. C., Dantuma, N. P., Katou, Y. et al.** (2014). The chromosomal association of the SMC5/6 complex depends on cohesin and predicts the level of sister chromatid entanglement. *PLoS Genet.* **10**, e1004680. doi:10.1371/journal.pgen.1004680
- Jimenez, D. S., Kim, J., Ragipani, B., Zhang, B., Street, L. A., Kramer, M., Albritton, S. E., Winterkorn, L. and Ercan, S.** (2021). Condensin DC spreads linearly and bidirectionally from recruitment sites to create loop-anchored TADs in *C. elegans*. *Biorxiv* 2021.03.23.436694.
- Kim, H.-S., Vanoosthuysen, V., Fillingham, J., Roguev, A., Watt, S., Kislinger, T., Treyer, A., Carpenter, L. R., Bennett, C. S., Emili, A. et al.** (2009). An acetylated form of histone H2A.Z regulates chromosome architecture in *Schizosaccharomyces pombe*. *Nat. Struct. Mol. Biol.* **16**, 1286–1293. doi:10.1038/nsmb.1688
- Kim, D., Perteau, G., Trapnell, C., Pimentel, H., Kelley, R. and Salzberg, S. L.** (2013). TopHat2: accurate alignment of transcriptomes in the presence of insertions, deletions and gene fusions. *Genome Biol.* **14**, R36. doi:10.1186/gb-2013-14-4-r36
- Kimura, H. and Cook, P. R.** (2001). Kinetics of core histones in living human cells: little exchange of H3 and H4 and some rapid exchange of H2b. *J. Cell Biol.* **153**, 1341–1354. doi:10.1083/jcb.153.7.1341
- Kimura, K. and Hirano, T.** (2000). Dual roles of the 11S regulatory subcomplex in condensin functions. *Proc. Natl. Acad. Sci. USA* **97**, 11972–11977. doi:10.1073/pnas.220326097
- Kinoshita, K., Kobayashi, T. J. and Hirano, T.** (2015). Balancing acts of two HEAT subunits of condensin I support dynamic assembly of chromosome axes. *Dev. Cell* **33**, 94–106. doi:10.1016/j.devcel.2015.01.034
- Kong, M., Cutts, E. E., Pan, D., Beuron, F., Kaliyappan, T., Xue, C., Morris, E. P., Musacchio, A., Vannini, A. and Greene, E. C.** (2020). Human condensin I and II drive extensive ATP-dependent compaction of nucleosome-bound DNA. *Mol. Cell* **79**, 99–114.e9. doi:10.1016/j.molcel.2020.04.026
- Kramer, M., Kranz, A.-L., Su, A., Winterkorn, L. H., Albritton, S. E. and Ercan, S.** (2015). Developmental dynamics of X-Chromosome dosage compensation by the DCC and H4K20me1 in *C. elegans*. *PLoS Genet.* **11**, e1005698. doi:10.1016/j.molcel.2020.04.026
- Kschonsak, M., Merkel, F., Bisht, S., Metz, J., Rybin, V., Hassler, M. and Haering, C. H.** (2017). Structural basis for a safety-belt mechanism that anchors condensin to chromosomes. *Cell* **171**, 588–600.e24. doi:10.1016/j.cell.2017.09.008
- Langmead, B. and Salzberg, S. L.** (2012). Fast gapped-read alignment with Bowtie 2. *Nat. Methods* **9**, 357–359. doi:10.1038/nmeth.1923
- Lau, A. C. and Csankovszki, G.** (2014). Condensin-mediated chromosome organization and gene regulation. *Front. Genet.* **5**, 473. doi:10.3389/fgene.2014.00473
- Lau, A. C., Nabeshima, K. and Csankovszki, G.** (2014). The *C. elegans* dosage compensation complex mediates interphase X chromosome compaction. *Epigenetics Chromatin* **7**, 31. doi:10.1186/1756-8935-7-31
- Lee, B.-G., Merkel, F., Allegritti, M., Hassler, M., Cawood, C., Lecomte, L., Reilly, F. J. O., Sinn, L. R., Gutierrez-Escribano, P., Kschonsak, M. et al.** (2020). Cryo-EM structures of holo condensin reveal a subunit flip-flop mechanism. *Nat. Struct. Mol. Biol.* **27**, 743–751. doi:10.1038/s41594-020-0457-x
- Liu, W., Tanasa, B., Tyurina, O. V., Zhou, T. Y., Gassmann, R., Liu, W. T., Ohgi, K. A., Benner, C., Garcia-Bassets, I., Aggarwal, A. K. et al.** (2010). PHF8 mediates histone H4 lysine 20 demethylation events involved in cell cycle progression. *Nature* **466**, 508–512. doi:10.1038/nature09272
- Love, M. I., Huber, W. and Anders, S.** (2014). Moderated estimation of fold change and dispersion for RNA-seq data with DESeq2. *Genome Biol.* **15**, 550. doi:10.1186/s13059-014-0550-8
- Mazza, D., Abernathy, A., Golob, N., Morisaki, T. and McNally, J. G.** (2012). A benchmark for chromatin binding measurements in live cells. *Nucleic Acids Res.* **40**, e119. doi:10.1093/nar/gks701
- Meyer, B. J.** (2005). X-Chromosome dosage compensation. In *WormBook* (ed. The *C. elegans* research community). Wormbook. doi:10.1895/wormbook.1.8.1
- Miller, S. A., Policastro, R. A., Savant, S. S., Sriramkumar, S., Ding, N., Lu, X., Mohammad, H. P., Cao, S., Kalin, J. H., Cole, P. A. et al.** (2020). Lysine-specific demethylase 1 mediates AKT activity and promotes epithelial-to-mesenchymal transition in PIK3CA-mutant colorectal cancer. *Mol. Cancer Res.* **18**, 264–277. doi:10.1158/1541-7786.MCR-19-0748
- Minnen, A., Bürmann, F., Wilhelm, L., Anchimiuk, A., Diebold-Durand, M.-L. and Gruber, S.** (2016). Control of SMC coiled coil architecture by the ATPase heads facilitates targeting to chromosomal ParB/parS and release onto flanking DNA. *Cell Reports* **14**, 2003–2016. doi:10.1016/j.celrep.2016.01.066
- Moore, B. T., Jordan, J. M. and Baugh, L. R.** (2013). WormSizer: high-throughput analysis of nematode size and shape. *PLoS ONE* **8**, e57142. doi:10.1371/journal.pone.0057142
- Mueller, F., Stasevich, T. J., Mazza, D. and McNally, J. G.** (2013). Quantifying transcription factor kinetics: at work or at play? *Crit. Rev. Biochem. Mol.* **48**, 492–514. doi:10.3109/10409238.2013.833891
- Nuebler, J., Fudenberg, G., Imakaev, M., Abdennur, N. and Mirny, L. A.** (2018). Chromatin organization by an interplay of loop extrusion and compartmental segregation. *Proc. Natl. Acad. Sci. USA* **115**, 201717730. doi:10.1073/pnas.1717730115
- Paul, M. R., Markowitz, T. E., Hochwagen, A. and Ercan, S.** (2018a). Condensin depletion causes genome decompaction without altering the level of global gene expression in *Saccharomyces cerevisiae*. *Genetics* **210**, genetics.301217.2018. doi:10.1534/genetics.118.301217
- Paul, M. R., Hochwagen, A. and Ercan, S.** (2018b). Condensin action and compaction. *Curr. Genet.* **65**, 407–415. doi:10.1007/s00294-018-0899-4
- Petty, E. L., Collette, K. S., Cohen, A. J., Snyder, M. J. and Csankovszki, G.** (2009). Restricting dosage compensation complex binding to the X chromosomes by H2A.Z/HTZ-1. *PLoS Genet.* **5**, e1000699. doi:10.1371/journal.pgen.1000699
- Piazza, I., Rutkowska, A., Ori, A., Walczak, M., Metz, J., Pelechano, V., Beck, M. and Haering, C. H.** (2014). Association of condensin with chromosomes depends on DNA binding by its HEAT-repeat subunits. *Nat. Struct. Mol. Biol.* **21**, 560–568. doi:10.1038/nsmb.2831
- Ramírez, F., Ryan, D. P., Grüning, B., Bhardwaj, V., Kilpert, F., Richter, A. S., Heyne, S., Dündar, F. and Manke, T.** (2016). deepTools2: a next generation web server for deep-sequencing data analysis. *Nucleic Acids Res.* **44**, W160–W165. doi:10.1093/nar/gkw257
- Ramírez, F., Bhardwaj, V., Arrigoni, L., Lam, K. C., Grüning, B. A., Villaveces, J., Habermann, B., Akhtar, A. and Manke, T.** (2018). High-resolution TADs reveal DNA sequences underlying genome organization in flies. *Nat. Commun.* **9**, 189. doi:10.1038/s41467-017-02525-w
- Ramirez-Gonzalez, R. H., Bonnal, R., Caccamo, M. and MacLean, D.** (2012). Bio-samtools: Ruby bindings for SAMtools, a library for accessing BAM files containing high-throughput sequence alignments. *Source Code Biol. Med.* **7**, 6. doi:10.1186/1751-0473-7-6
- Schindelin, J., Arganda-Carreras, I., Frise, E., Kaynig, V., Longair, M., Pietzsch, T., Preibisch, S., Rueden, C., Saalfeld, S., Schmid, B. et al.** (2012). Fiji: an open-source platform for biological-image analysis. *Nat. Methods* **9**, 676–682. doi:10.1038/nmeth.2019
- Schmitz, M. L., Higgins, J. M. G. and Seibert, M.** (2020). Priming chromatin for segregation: functional roles of mitotic histone modifications. *Cell Cycle* **19**, 625–641. doi:10.1080/15384101.2020.1719585
- Sheikh, B. N., Guhathakurta, S. and Akhtar, A.** (2019). The non-specific lethal (NSL) complex at the crossroads of transcriptional control and cellular homeostasis. *EMBO Rep.* **20**, e47630. doi:10.15252/embr.201847630

- Stiernagle, T.** (2006). Maintenance of *C. elegans*, WormBook (ed. The *C. elegans* Research Community), <http://www.wormbook.org>. doi:10.1895/wormbook.1.101.1
- Street, L. A., Morao, A. K., Winterkorn, L. H., Jiao, C.-Y., Albritton, S. E., Sadic, M., Kramer, M. and Ercan, S.** (2019). Binding of an X-specific condensin correlates with a reduction in active histone modifications at gene regulatory elements. *Genetics* **212**, genetics.302254.2019. doi:10.1534/genetics.119.302254
- Swygart, S. G., Kim, S., Wu, X., Fu, T., Hsieh, T.-H., Rando, O. J., Eisenman, R. N., Shendure, J., McKnight, J. N. and Tsukiyama, T.** (2019). Condensin-dependent chromatin compaction represses transcription globally during quiescence. *Mol. Cell* **73**, 533-546.e4. doi:10.1016/j.molcel.2018.11.020
- Tada, K., Susumu, H., Sakuno, T. and Watanabe, Y.** (2011). Condensin association with histone H2A shapes mitotic chromosomes. *Nature* **474**, 477-483. doi:10.1016/j.molcel.2011.11.020
- Tanaka, A., Tanizawa, H., Sriswasdi, S., Iwasaki, O., Chatterjee, A. G., Speicher, D. W., Levin, H. L., Noguchi, E. and Noma, K.** (2012). Epigenetic regulation of condensin-mediated genome organization during the cell cycle and upon DNA damage through histone H3 lysine 56 acetylation. *Mol. Cell* **48**, 532-546. doi:10.1016/j.molcel.2012.09.011
- Thadani, R., Kamenz, J., Heeger, S., Muñoz, S. and Uhlmann, F.** (2018). Cell-cycle regulation of dynamic chromosome association of the condensin complex. *Cell Reports* **23**, 2308-2317. doi:10.1016/j.celrep.2018.04.082
- Uhlmann, F.** (2016). SMC complexes: from DNA to chromosomes. *Nat. Rev. Mol. Cell Biol.* **17**, 399-412. doi:10.1038/nrm.2016.30
- Vian, L., Pekowska, A., Rao, S. S. P., Kieffer-Kwon, K.-R., Jung, S., Baranello, L., Huang, S.-C., Khattabi, L. E., Dose, M., Pruett, N. et al.** (2018). The energetics and physiological impact of cohesin extrusion. *Cell* **173**, 1165-1178.e20. doi:10.1016/j.cell.2018.03.072
- Vielle, A., Lang, J., Dong, Y., Ercan, S., Kotwaliwale, C., Rechtsteiner, A., Appert, A., Chen, Q. B., Dose, A., Egelhofer, T. et al.** (2012). H4K20me1 contributes to downregulation of X-linked genes for *C. elegans* dosage compensation. *PLoS Genet.* **8**, e1002933. doi:10.1371/journal.pgen.1002933
- Walther, N., Hossain, M. J., Politi, A. Z., Koch, B., Kueblbeck, M., Ødegård-Fougner, Ø., Lampe, M. and Ellenberg, J.** (2018). A quantitative map of human Condensins provides new insights into mitotic chromosome architecture. *J. Cell Biol.* **217**, 2309-2328. doi:10.1083/jcb.201801048
- Wells, M. B., Snyder, M. J., Custer, L. M. and Csankovszki, G.** (2012). *Caenorhabditis elegans* dosage compensation regulates histone H4 chromatin state on X Chromosomes. *Mol. Cell Biol.* **32**, 1710-1719. doi:10.1128/MCB.06546-11
- Wilhelm, L., Buermann, F., Minnen, A., Shin, H.-C., Toseland, C. P., Oh, B.-H. and Gruber, S.** (2015). SMC condensin entraps chromosomal DNA by an ATP hydrolysis dependent loading mechanism in *Bacillus subtilis*. *eLife* **4**, e06659. doi:10.7554/eLife.06659
- Wolff, J., Bhardwaj, V., Nothjunge, S., Richard, G., Renschler, G., Gilsbach, R., Manke, T., Backofen, R., Ramírez, F. and Grüning, B. A.** (2018). Galaxy HiCExplorer: a web server for reproducible Hi-C data analysis, quality control and visualization. *Nucleic Acids Res.* **46**, gky504. doi:10.1093/nar/gky504
- Wolff, J., Rabbani, L., Gilsbach, R., Richard, G., Manke, T., Backofen, R. and Grüning, B. A.** (2020). Galaxy HiCExplorer 3: a web server for reproducible Hi-C, capture Hi-C and single-cell Hi-C data analysis, quality control and visualization. *Nucleic Acids Res.* **48**, W177-W184. doi:10.1093/nar/gkaa220
- Wood, A. J., Severson, A. F. and Meyer, B. J.** (2010). Condensin and cohesin complexity: the expanding repertoire of functions. *Nat. Rev. Genet.* **11**, 391-404. doi:10.1038/nrg2794
- Wu, Y., Han, B., Gauvin, T. J., Smith, J., Singh, A. and Griffin, E. E.** (2019). Single-molecule dynamics of the P granule scaffold MEG-3 in the *Caenorhabditis elegans* zygote. *Mol. Biol. Cell* **30**, 333-345. doi:10.1091/mbc.E18-06-0402
- Yonker, S. A. and Meyer, B. J.** (2003). Recruitment of *C. elegans* dosage compensation proteins for gene-specific versus chromosome-wide repression. *Development* **130**, 6519-6532. doi:10.1242/dev.00886
- Yoshimura, S. H. and Hirano, T.** (2016). HEAT repeats - versatile arrays of amphiphilic helices working in crowded environments? *J. Cell Sci.* **129**, 3963-3970. doi:10.1242/jcs.185710
- Yuen, K. C., Slaughter, B. D. and Gerton, J. L.** (2017). Condensin II is anchored by TFIIIC and H3K4me3 in the mammalian genome and supports the expression of active dense gene clusters. *Sci. Adv.* **3**, e1700191. doi:10.1126/sciadv.1700191